

Graphical Abstract

Tracking Meltpool Dynamics and Interfacial Intermetallic Grains in Laser-Processed Ti-Au system: A Non-isothermal Phase Field Approach

Upadesh Subedi, Nele Moelans, Tomasz Tański, Anil Kunwar

Highlights

Tracking Meltpool Dynamics and Interfacial Intermetallic Grains in Laser-Processed Ti-Au system: A Non-isothermal Phase Field Approach

Upadesh Subedi, Nele Moelans, Tomasz Tański, Anil Kunwar

- Composition and thermal fields constituting the driving force.
- Feauturing meltpool dynamics and intermetallic grains evolution.
- Linking process parameters to the material structure evolution.
- Methodology to distinguish thermal and chemical diffusion fronts.

Tracking Meltpool Dynamics and Interfacial Intermetallic Grains in Laser-Processed Ti-Au system: A Non-isothermal Phase Field Approach

Upadesh Subedi^{a,b,c,*}, Nele Moelans^c, Tomasz Tański^a and Anil Kunwar^b

^aDepartment of Engineering Materials and Biomaterials, Faculty of Mechanical Engineering, Silesian University of Technology, 44-100 Gliwice, Poland

^bScientific and Didactic Laboratory of Nanotechnology and Material Technologies, Faculty of Mechanical Engineering, Silesian University of Technology, 44-100 Gliwice, Poland

^cDepartment of Materials Engineering, KU Leuven, Kasteelpark Arenberg 44 Bus 2450, 3001 Leuven, Belgium

ARTICLE INFO

Keywords:

Interdiffusion
Laser irradiance
Non-isothermal phase field model
Interfacial Reaction
Lewis number

ABSTRACT

This study explores the dynamics of laser-induced phase transitions and microstructural evolution in the Ti-Au alloy system, crucial for advancing additive manufacturing processes. By varying laser parameters, including irradiance and scan speed, we quantified phase areas and free energy dynamics, revealing intricate interplays between thermal and phase diffusion. Notable findings include: Under maximum heat flux conditions (150 kW/cm^2 at 4 nm/ms), melt pool depth reached 180.12 nm , surpassing the 158.3 nm depth observed at 134.6 kW/cm^2 . The growth of Ti_3Au intermetallic compound (IMC) formed due to the interfacial reaction was studied. IMC layer thickness peaked at 364.32 nm under higher irradiance, marking a 25.68% increase over lower irradiance conditions. Analysis of Lewis Number unveiled the slower diffusion of the melt pool compared to thermal diffusion. These insights offer predictive control over melt pool morphology and phase evolution, guiding the optimization of laser processing techniques. Our work lays the groundwork for refining phase field models and enhancing 3D printing of biomaterials, promising advancements in various industrial applications.

1. Introduction

Titanium alloys have been ubiquitously used as one of the key materials in modern manufacturing processes. Due to their heightened superior qualities such as high-strength-to-weight ratio [1], lightweight, corrosion resistance [2], enhanced mechanical properties [3] and above all the bio-compatibility [4]. Lately, the research community is more focused on titanium-gold (Ti-Au) binary alloy. Titanium alloyed with gold results into a highly superior material that has a huge application in medical sector especially as a bio-implant material [5]. The inert nature of gold alloyed with superior mechanical properties of titanium gives result into an unique combination of strength, non-toxicity, corrosion-resistance, high radiopacity as well as showcasing the shape memory effect [6]. In addition, the improved integration of alloy with bone tissue makes it highly suitable for bodily implant resulting in faster and reliable osseointegration [7, 8].

In recent study, Svanidze et al. [9] reported that an intermetallic compound (IMC) of Titanium-Gold (Ti_3Au) exhibits an exceptional hardness nearly four times as that of pure Ti or steel alloys. Similarly, Lukose et al. [10] found that Ti_3Au thin film not only shows high hardness but also an excellent bio-compatibility with viability level greater than 95% suggesting it as the future of thin film coating capable of expanding lifetime of bodily implants. In another work by Kocabas et al. [11], the intermetallics Ti_3Au showed a remarkable enhancement of energy absorption in thin-walled tubes under different impact loading.

With such incredible physical and mechanical properties, the practical application of the intermetallics Ti_3Au comes to the challenge of manufacturing it with purity. A few methods have been used to produce Ti_3Au intermetallics samples on small quantities for purely research purposes such as, Svanidze et al. used arc melting method with several remelting cycles. Similarly, magnetron sputtering with a Nano PVD deposition has been used to create Ti_3Au on a $\text{Ti}_6\text{Al}_4\text{V}$ substrate [10, 12, 13] on a nanoscale. In a study by Bialas et al. [5], the development of Ti_3Au was carried

 upadesh.subedi@polsl.pl (U. Subedi)

ORCID(s): 0000-0002-5527-1348 (U. Subedi); 0000-0003-3361-2954 (N. Moelans); 0000-0003-4024-1231 (T. Tański); 0000-0003-4295-5772 (A. Kunwar)

out by electrochemical coating of titanium on a gold layer with additional heat deposition from laser to induce the intermetallics at the Ti-Au interface.

The advancement in complex yet miniaturized product development has lead to a chain reaction in innovation of advanced manufacturing techniques such as nano-structure fabrication producing nanoparticles, nano-wires and nano-tubes along with the 3D nano-structures [14]. With an advancement in nano-scale technologies following the empirical Moore's law [15], the effect of miniaturization in transistors on an integrated circuit has created a cascade effect on all the aspects of modern product-development ecosystem making them smaller, lighter compact and highly energy efficient [16]. As the product gets smaller and compact the need of cutting-edge advanced manufacturing techniques that can operate in nano-scale with high precision and accuracy becomes evident. With an extreme control over the processing parameters and nano-scale localized energy deposition, laser technology has evolved as one of the primary method of nano-material processing. Previously, lasers were preferred choice for a top-down approach of material processing for material removal and machining using methods such as ion beam, ion etching, laser ablation while the nano-fabrication was carried out with bottom-up approach to obtain nano-structures via deposition atoms and molecules with vapor deposition techniques [17, 18, 19]. But lately, with the technological advancement of nano-scale ultra fast lasers, the pulsed laser deposition, laser chemical vapor deposition and nano-additive manufacturing has become possible to fabricate nano-structures of high dimensional accuracy [20, 21, 22]. The ultra-fast lasers enables nano-scale energy deposition minimizing thermal effects on surrounding materials and preserves the nano-structure's integrity [23]. This approach of precise control over the temperature fields and heating mechanism enables the nucleation and growth of nanostructures with a high spatial accuracy [24]. The latest nano-manufacturing techniques such as: multiphoton polymerization, multiphoton photoreduction, nano-welding, nano-forming has further shaped the way of fabricating 3D nanostructures with high spatial resolution aiding to the application of laser in nano-scale additive manufacturing [25]. Deep ultra-violet laser source are used to produce 90nm-130nm lines in lithography whereas, femto second pulsed laser has been used for nano-resolution fabrication with ablation threshold setting to that of Gaussian beam profile. These ultra-fast lasers have been used to create nano-features such as pits, voids, strips, ripples, lines in the nano-scale well below 100nm in dimensions [14, 26]. With the development of lasers that can accurately and precisely deposit heat at nano-scale the use of such technology becomes evident in additive manufacturing of nano-materials with nano-structures. From the laser deposition of nano-particles to supply the localized thermal energy at nano-scale enhancing the growth of nano-structures, the application of latest ultrafast laser devices are going to play a major role in nano-additive manufacturing.

As the additive manufacturing (AM) technologies have started to replace the mainstream manufacturing methods and prototype development, the different aspects of AM methods can be employed in sectors requiring rapid, agile and reliable product [27, 28, 29]. Additionally, the real world application of Ti-Au alloys in multi-disciplinary industrial area such as aerospace, automotive, energy, medical, marine, and chemical processing is broadening.[30, 31, 32, 33, 34, 35, 3, 36, 37]. With multiple AM techniques as Selective Laser Melting (SLM) [38], Selective Laser Sintering (SLA) [39], and Directed Energy Deposition (DED) [40] the window of possibilities are wide open where one can perform rapid prototyping to the development of industrial standard highly customized and complex geometries in within hours. In addition to these versatile technologies, utilizing the latest machine learning toolkits [41, 42, 43] the physical as well as mechanical properties can be pre-calculated and predicted offering an unprecedented control over the complex design and material properties to level of the microstructural growth.

As described by Nohrira et. al, [6], with specific heat treatment of Ti-Au binary system, it can produce the Ti_3Au intermetallics with desired mechanical properties. And by utilizing a focused energy beam, a precise, repeatable and high control over the microstructure along with the mechanical properties can be attained via the additive manufacturing technologies [44, 45]. With this insight we extend the horizon of growth evolution of Ti_3Au intermetallics grains with the computational study of application of laser heat source in this work. With a detailed analysis of laser processing parameter's effect on microstructure evolution, our work primarily focus on effects of two variables: laser scan speeds and laser irradiation on IMC grain growth. Similarly, we explore the laser-meltpool characteristics, temperature-composition dependent free-energy driving the phase transitions, thermal history of the system, and further proceed to quantify the lead-lag dynamics between phase and thermal diffusions in-terms of a dimensionless scalar value called Lewis number [46].

In order to track the growth evolution of microstructure and phase transitions due to the influence of laser irradiation in the computational domain, Phase Field (PF) diffused interface model is employed with multiple physics coupled tightly. A number of PF models and techniques exists in literature such as entropy functional [47], free energy functional [48, 49], and grand potential functional [50] for microstructure evolution study. Our model consists of phase-field

variables evolving spatio-temporally described by a set of partial differential equations dictating the changes in system's phases. And the driving force for these changes depends upon the free-energy functional, temperature and composition [51] of individual phases.

Since, PF method serves as an excellent computational tool tracking the microstructure evolution, it has gained significant attention in modelling additive manufacturing processes. Phase field modelling of such process involving the melting, solidification and grain growth can be established by coupling the heat transfer and fluid flow physics with it. Gong et al. [52] studied solidification and dendrite growth during the electron beam additive manufacturing (EBAM) of Ti-6Al-4V alloy. Although their work claims to show grain growth comparable to experimental results, their model lacks several essential parameters for accurately representing the phenomenon. Their binary approximation of a ternary system and the absence of fluid-flow coupling to the phase-field model, assuming a flow-less melt pool regime, are significant limitations. Additionally, their assumption of a uniform temperature within individual phases makes it a constant temperature model. The composition dependence of free energy is restricted to two constant composition values for solid and liquid phases, using a double-well approximation. Liu et al. [49] combined the phase-field method with the lattice Boltzmann method to simulate dendrite growth, heat transfer, and fluid flow during the additive manufacturing process involving Ti-6Al-4V alloy. Despite claiming a tight coupling of the two methods, their model lacks composition-temperature dependence of the free energies of the individual phases. For the phase field simulation, two fixed temperatures are considered: 1878 K for the solid phase and 1928 K for the liquid phase. They further assume constant material properties throughout the non-isothermal process, and employ a pseudo-binary approach for modeling a ternary alloy system. A similar approach for simulating microstructural evolution during the EBAM process of Ti-6Al-4V alloy is found in the work by Sahoo et al. [53] work. Their model also uses a binary approximation of a ternary alloy system and lacks fluid-flow coupling. The constant values for thermophysical properties reduce the model's reliability, as thermodynamic processes such as solidification and phase transition depend on material properties that fluctuate with temperature. Darabi et al. [54] presented a multi-scale, multi-physics model of powder bed fusion of Inconel-625. Their model includes the coupling of elasticity with the phase-field method but the coupling of thermal history with the phase-field lacks continuous temperature dependence of free energy. They have used two fixed temperatures for the molten and solidified phases each, without consideration of flow within the melt pool. Similarly, their work assumes constant material properties (such as: thermal conductivity, density, specific heat capacity) within a phase, ignoring the temperature dependence of material properties. The assumption of powder alloy as a single-component system further overlooks interdiffusion effects and, the formation and growth of intermetallics. Yang et al. [47] simulated microstructure evolution during the selective laser sintering (SLS) process using phase-field modeling for stainless steel (316L) powder. Their model does not consider the role of steel alloy's phase composition regarding its influencing the evolution pattern. In reality the phase field model for a binary or multi-component alloy should be different to that of pure metal [55]. The alloy model is infact the significant expansion of pure material model as the former must account for the composition dependence of the alloy phase not only at the bulk but also at the interface. In phase field modeling of laser processed alloys, the free energy term should account for both composition and temperature. Our present model meticulously blends the compositional and thermal field to describe the microstructure evolution, thereby becoming novel work by accounting for the material phase composition in laser processed non-isothermal condition.

The formation of intermetallics at the Ti-Au interface occurs via the following exothermic thermo-chemical reaction:



Where, $\Delta H_f^{Ti_3Au}(T)$ is the enthalpy of formation for Ti_3Au intermetallic from the constituent species Ti and Au at temperature T. During laser processing it is known that the interface experiences temperature fluctuations and so it is necessary to consider the $\Delta H_f^{Ti_3Au}$ for reactions at different temperatures as following [56, 57]:

$$\Delta H_f^{Ti_3Au}(298K) = -31.39 \text{ kJ/mol}$$

$$\Delta H_f^{Ti_3Au}(750K) = -17.91 \text{ kJ/mol}$$

$$\Delta H_f^{Ti_3Au}(1000K) = -10.46 \text{ kJ/mol}$$

In all these three temperatures, Ti_3Au formation is thermodynamically stable and this interfacial reaction can proceed along the Ti-Au interface. However, the stability of Ti_3Au is guaranteed only below 1350.9K (critical temperature) [56, 57]. Through the thermochemical reaction at the interface in a temperature range between 300 K to 1350.9 K, the Ti_3Au intermetallic nucleates and grows subsequently. After reaching the critical nucleation radius the intermetallic starts to grow as grains. Our present work describes such growth of the grains (product of interfacial reactions) under non-isothermal conditions and stands out as one of the seminal models of such interfacial phenomena. Here, we present a multi-phase, multi-physics phase-field model of laser processing for the Ti-Au binary alloy system. Our model fully couples phase-field equations with heat transfer and fluid flow physics, offering a unique perspective on the dynamics of phase transition. We specifically address the dynamic nature of the melt pool and Ti_3Au intermetallic growth at the interface, considering interdiffusion effects. This study advances previous models by incorporating temperature-composition-dependent free energy functionals for individual phases and temperature-dependent material properties. We provide a comprehensive study and quantification of dynamic microstructure evolution and phase transition during laser treatment for a set of key laser processing parameters (irradiance and scanning speed). Detailed analyses include the evolution of phase areas, melt pool depth and width, intermetallic grain thickness, and phase stability between the melt pool and heat-affected zone.

Additionally, we introduce a novel approach to measure the difference between thermal and phase diffusion by defining their values in units of time, termed "*Positional Time Lag* (δt_{pos})."
This phenomenon arises because the thermal diffusion front travels faster than the melt pool phase front [58]. We further quantify this using the non-dimensional Lewis Number, which provides a ratio of thermal to phase diffusion [46]. Our work incorporates these quantities to study the effects of laser processing parameters on the relative propagation of thermal and phase diffusion fronts. We employ the Finite Element Method (FEM) for discretization and conducted our simulations using the open-source FEM solver MOOSE Framework [59, 60, 61], which utilizes the PJFNK (Preconditioned Jacobian-Free Newton Krylov) solver for iteratively solving coupled non-linear partial differential equations. Our study leverages the MOOSE framework and the Phase Field method to simulate interdiffusion effects in multiphase, multicomponent systems by utilizing the KKS model [55] to ensure chemical potential equilibrium at phase boundaries, our approach demonstrates superior performance, particularly in multicomponent systems.

2. Multi-Physics Multi-Phase Field Formulation

Laser processing in an additive manufacturing process is inherently an unsteady and transient phenomenon [62]. Designing an accurate computational model to replicate the intricate events during laser treatment requires solving coupled partial differential equations governing a set of multiphysics. In our study we developed such multi-physics model coupling phase-field, heat transfer and fluid flow equations describing the nature of phase-field variables, heat deposition and distribution and flow dynamics inside meltpool. In a multi-phase Au-Ti system, the phase-field variables of concern are: composition (a conserved quantity) and order-parameters (a non-conserved quantity) that evolves in the domain driven by the free energy of the system. The following sections discuss the individual physical phenomena, the coupled equations, and the temperature-dependent material properties associated with each phase.

2.1. Phase Field Equations

In a system initially consisting of three phases: Ti-rich HCP (Hexagonal Closed Packed) at the bottom, Au-rich FCC (Face Centered Cubic) solid at the top, and 4 IMC grains at the interface, the introduction of a laser at the top immediately adds a fourth phase, Au-rich LIQUID, as illustrated in Figure 1b. A computational model with dimensions of $1300\text{ nm} \times 500\text{ nm}$ in the x-z direction was designed for non-isothermal phase-field modelling. The initial area of each phases taken into consideration are, HCP: $1.3 \times 10^5\text{ nm}^2$, FCC: $3.45 \times 10^5\text{ nm}^2$, LIQUID: $1.0 \times 10^4\text{ nm}^2$. and IMC grains combined: $1.65 \times 10^5\text{ nm}^2$.

In a binary system (Ti-Au), composition of single element is sufficient to describe the conserved phase-field variable as the molar fraction of Au and Ti in a phase sums to 1. Here, we take the molar fraction of 'Au' (c^{Au}) as 'c' to represent the composition of the phase, with c_{HCP} , c_{IMC} , c_{LIQ} and c_{FCC} denoting the molar fraction of Au in HCP, IMC, LIQUID and FCC phases respectively. For the non-conserved variables representing HCP, FCC, LIQUID and 4 grains of IMC phases we defined a total of 7 order-parameters. These order-parameters are denoted as η_i with the value set to 1 if they are inside their corresponding phase and 0 outside their phase. Here, we have defined the 7 order-parameters as: η_1 for HCP phase, η_2 , η_3 , η_4 and η_5 for 4 grains of IMC phase, η_6 for LIQUID phase and η_7 for FCC phase. The schematics of our computational domain showcasing the 4 phases and 7 order parameter system is shown in Figure 1b.

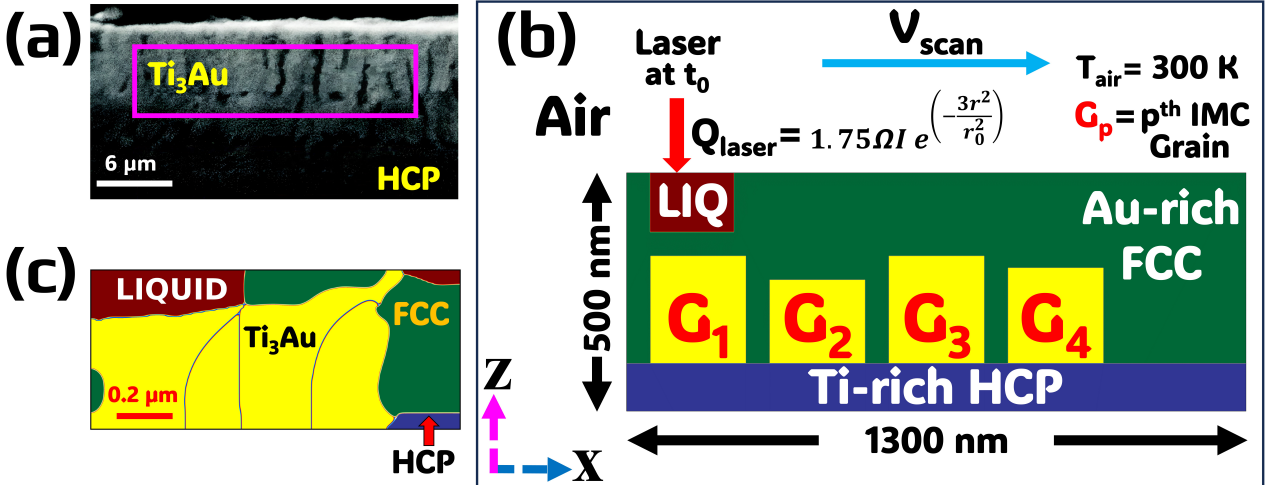


Figure 1: (a) Experimental microstructural image depicting Ti₃Au intermetallics (highlighted within magenta rectangle) formed in the aftermath of laser treatment for an Au-coated Ti film [5]. Captured post-cooling, the highlighted region showcases the formation of Ti₃Au intermetallic phase at the expense of Au-rich FCC and Ti-rich HCP phases. The dark region at the bottom of the image represents HCP region (rich in Titanium). (b) Schematic representation of simulation setup for laser-induced heat treatment in a multiphase Ti-Au domain (1300 nm × 500 nm) comprising of four distinct phases: Ti-rich HCP, Ti₃Au IMC, Au-rich FCC, and LIQUID. A Gaussian laser heat source (depicted by the red arrow) is dynamically applied to the top layer, initially positioned at a horizontal distance of 125 nm from the left. The scanning speed of the laser is denoted as v_{scan}, and G_p signifies the pth IMC grain. (c) Snapshot, taken at 355.78 ms into simulation, provides a glimpse of ongoing laser treatment (I: 150 kW/cm²; v_{scan}: 4 nm/ms) with beam already crossing the right end. Noteworthy in this image is the discernible growth of IMC grains, manifesting in irregular and distinct shapes. This observation aligns with our previous experimental findings [5], underscoring the accuracy and relevance of the simulation in capturing the dynamic evolution of IMC grains during the laser processing.

In a multi-phase system undergoing laser-induced phase transitions, there is constant interaction between distinct phases at the interface. This necessitates the use of an interpolation function to accurately interpolate the temperature-dependent material properties and characteristics between the co-existing phases. We have employed a thermodynamically consistent function ($h_i(\eta)$) introduced by Moelans [63] for the purpose. The corresponding interpolation function for phases with a single grain (HCP, FCC, and LIQUID), and for the multiple grains of IMC phase is given by Equation 1 [51].

$$h_i = \begin{cases} \frac{\eta_i^2}{N} & ; \text{HCP, FCC, LIQUID} \\ \sum_{k=1}^p \eta_k^2 & ; \text{IMC} \end{cases} \quad (1)$$

In the above equations, N represents the total order parameters, and *i* denotes the distinct phases. The order-parameters for HCP, FCC, and LIQUID is given by the variable η_i , while for IMC grains, it is expressed as $\eta_{i,j}$. When an external source of heat is applied to the computational domain, morphological changes in the microstructure become evident caused by the system's free energy driving the transformations. To numerically model the physical

Table 1

Tabulated coefficients of composition-temperature dependent Gibbs Free Energy, expressed through higher-order polynomial functions across distinct phases.

Coeff \ Phases	HCP	IMC	LIQ	FCC
F_i	1000	1000	11.599	19.858
$A_i(\text{J/mol})$	655.124	2328.75	30013.79	208000.75
$B_i(\text{J/mol.K}^n)$	9.225×10^{-6}	2.2×10^{-5}	0.00122	0.001463
$C_i(\text{J/mol.K})$	0	0	-0.75	-0.75
$D_i(\text{J/mol})$	-6.95	-12.6	-21	-5.8
c_{eq}^i	0.1015	0.261	0.5272	0.627
T_{eq}^i	1100	859.11	1939.34	593.26
m	2	2	4	6
n	2	2	2	2

behaviour of the microstructure, we incorporate the total free energy of the system as (F_{total}) in our model. This is achieved by combining the bulk free energy (F_{bulk}) and interfacial free energy (F_{int}) as follows:

$$F_{total} = F_{bulk} + F_{int} = \int_V (f_{bulk} + f_{int}) dV \quad (2)$$

In Equation 2, the bulk and interfacial energies are expressed in terms of free energy densities, i.e., energy per unit molar volume. The first term, bulk free energy density (f_{bulk}) incorporates the chemical- plus thermo- diffusional aspects and is expressed in Equation 3.

$$f_{bulk} = \sum_i h_i f_{bulk}^i = \sum_i \frac{G_i(c, T)}{V_m} \quad (3)$$

where terms h_i and f_{bulk}^i represent the interpolation function and the chemical bulk free energy density of phase "i", respectively. The molar volume V_m is assumed to be the same for all phases, taken as $10.21 \text{ cm}^3/\text{mol}$ (the V_m of Au) [64]. The notation $G_i(c, T)$ denotes the composition-temperature dependent molar Gibbs free energy of phase i . Due to thermal fluctuations induced by the laser within the computational domain, the molar Gibbs free energy of the system must accurately reflect thermodynamic changes associated with a variable temperature field. This necessitates considering both the thermal alterations (T) and the composition (c) to be incorporated in the free energy expressions as presented in Equation 4 represented by a higher-order polynomial function. The 3D visualization of free energy function for individual phases is shown in Figure 2e with composition and temperature represented on x and y axis respectively whereas, color indicating the value of free energy as a third dimension.

$$G_i = F_i \left[A_i(c_i - c_{eq}^i)^m + B_i(T - T_{eq}^i)^n + C_i c_i T + D_i \right] \quad (4)$$

where T represents the temperature and c_i denotes the composition of phase 'i'. The coefficients $F_i, A_i, B_i, C_i, D_i, a_i, b_i, c_{eq}^i, T_{eq}^i, m$ and n are fitted from the thermodynamical database (.TDB file) [65]. The values and units of these coefficients are presented in Table 1. It is to be noted that this equation incorporates the effect of both chemical and thermal diffusions in the multi-phase system. The cross-effect of T-variable on the spatial distribution of composition is briefly outlined later in Section 3.

The interfacial free energy density (f_{int}) in Equation 2 is mathematically expressed in Equation 5.

$$f_{int} = m f_{barrier} + \frac{\kappa}{2} \sum_i (\nabla \eta_i)^2 \quad (5)$$

Here, the model parameter term m and κ are associated with the diffused interface width (δ) and interfacial energy $\sigma [\text{J/m}^2]$ as described in the following Equations 6 and 7.

$$m = 6 \times \frac{\sigma}{\delta} \quad (6)$$

$$\kappa = \frac{3}{4} \times \delta \sigma \quad (7)$$

In this work, we take the values of δ and σ as 10 nm and 0.5 J/m² respectively [66]. The $f_{barrier}$ term of Equation 5 is a Landau polynomial of the phase field variable in 4th order which is expressed as Equation 8.

$$f_{barrier} = \sum_i \left(\frac{(\eta_i)^4}{4} - \frac{(\eta_i)^2}{2} \right) + \gamma \sum_i \sum_{j \neq i} \eta_i^2 \eta_j^2 + \frac{1}{4} \quad (8)$$

The phase-field simulation of laser-induced microstructural transformation can be simply understood as a mathematical system monitoring the spatio-temporal changes of conserved (c) and non-conserved (η) variables. For the conserved variable (c), its progression is tracked by Equation 9.

$$\frac{\partial c}{\partial t} = \nabla \cdot \left(\sum h_i M_i(T) \right) \nabla \left(\frac{\partial f_{bulk}}{\partial c_i} \right) - \vec{u} \cdot \nabla c_i \quad (9)$$

where, $M_i(T)$ is the temperature-dependent mobility of the i^{th} phase. Its value increases exponentially with the rise in temperature (Figure 2d), directly influencing the phase growth kinetics. The symbol \vec{u} vector denotes the velocity of molten alloy in the LIQUID phase. The Cahn-Hilliard phase mobility $M_i(T)$ is related to the phase diffusivity $D^i(T)$, thermodynamic factor A^i and grain boundary mobility (M_{gb}) as follows:

$$M_i(T) = \frac{D_i(T)}{A_i} + \sum_{j \neq i} h_j M_{gb} \quad (10)$$

Phase diffusivity governs the diffusion of phases from higher to lower concentrations over space and time within the computational domain, influenced by the temperature and composition gradients. The thermodynamic factor is a second-order partial derivative of bulk free energy density with respect to the composition, given as $A_i = \frac{\partial^2 f_{bulk}(T)}{\partial(c_i)^2}$. The term M_{gb} is interconnected with the grain-boundary diffusivity (D_{gb}), phase-specific thermodynamic factors, and the width of the grain boundary channel (δ_{gb}) between two adjacent grains. The expression for M_{gb} is given in Equation 11 [67].

$$M_{gb} = 3 \frac{D_{gb} \delta_{gb}}{(h_i A_i + h_j A_j) \delta} \quad (11)$$

Here, the value of δ_{gb} is taken as 0.5 nm. For the model's simplicity, we have considered M_{gb} to be one hundred times the value of IMC bulk phase's mobility [68].

The spatio-temporal evolution of the non-conserved phase-field variable (order-parameters) dictating the phase morphology is expressed in Equation 12 [51].

$$\frac{\partial \eta_i}{\partial t} = -L(\eta_1, \dots, \eta_N) \left(\frac{\partial f_{bulk}}{\partial \eta_i} - \nabla \cdot \frac{\partial f_{int}}{\partial \nabla \eta_i} \right) \quad (12)$$

where, $L(\eta_1, \dots, \eta_N) = L_i$ is defined in Equation 13.

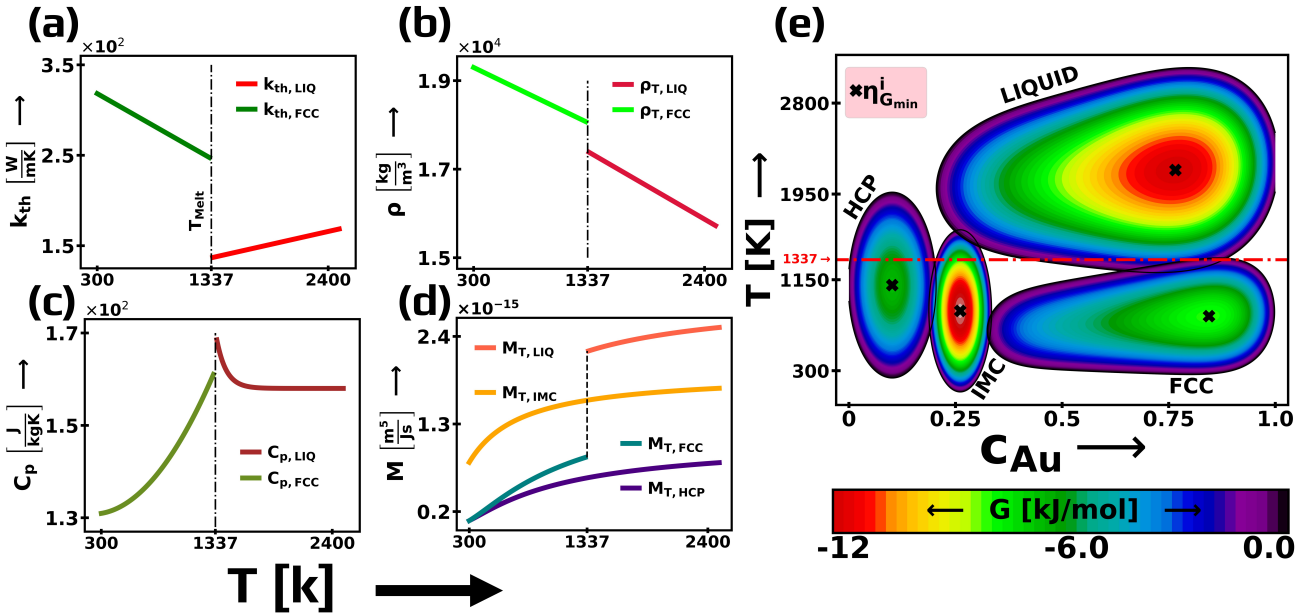


Figure 2: Considering temperature dependence of material properties to model transient and non-uniform heating. (a) The graph illustrates the linear decrease in thermal conductivity for the FCC phase from ambient conditions to its melting point at 1337K, whereas for the LIQUID phase, the thermal conductivity is rising. In (b) the density-temperature relationships are explored. Both LIQUID and FCC phases exhibit a linear decrease in density with increasing temperature. Notably, the LIQUID phase displays a steeper slope, indicating its distinctive response to temperature variations. Image (c) introduces the non-linear nature of specific heat capacity against temperature. While the FCC phase demonstrates an increasing trend, the LIQUID phase exhibits exponential decay. The Au-rich LIQUID and FCC phases, being located on top of computational domain and thus at proximity to laser heat source, are characterized by larger ΔT as compared to distinctly located Ti-rich IMC and HCP phases. So, k_{th} , ρ and C_p are assumed T-dependent for FCC and LIQUID phases, where constant for IMC and HCP phases. Plot (d) shows the temperature dependent mobility dynamics of all four HCP, IMC, LIQUID, and FCC phases. As M^i for all η s are exponentially increasing with T , all the four phases are assigned with T-dependent mobilities. Contour plot (e) depicts the dynamic behavior of Gibbs free energy concerning composition and temperature, unveiling the factors influencing phase growth and stability. Notably, the LIQUID phase emerges as the predominant stable state during laser-induced melting, followed closely by the IMC phase. As the laser advances, the LIQUID phase at any spatial point tends to solidify back to the FCC phase when the temperature falls below the melting, unless the IMC phase is present nearby. In such cases, the IMC phase supersedes FCC solidification, propelled by its second-lowest free energy. This complex interaction gives rise to a fascinating sequence of phase transitions.

$$L_i = \frac{\sum_{i=1}^N \sum_{j>1}^N L_{ij} \eta_i^2 \eta_j^2}{\sum_{i=1}^N \sum_{j>1}^N \eta_i^2 \eta_j^2} \quad (13)$$

here, L_{ij} is the interfacial mobility that is approximated as Equation 14.

$$L_{ij} = \frac{4m}{3\kappa} \times \frac{1}{\Omega_{ij}} \quad (14)$$

The term Ω_{ij} is a Cahn-Hilliard mobility dependent quantity which is approximated as:

$$\frac{1}{\Omega_{ij}} = \frac{M_i(T) + M_j(T)}{2 \times \tau} \quad (15)$$

where M_i and M_j are the temperature-dependent mobilities of phases i and j respectively. The parameter τ , represents the magnitude of Gibbs free energy's projection on the composition axis among interacting phases.

2.2. Energy Equation

In an iso-thermal system with laser source depositing the thermal energy dictating phase changes, the distribution of heat across the domain is given by Expression 16.

$$\rho_i C p_i \left(\frac{\partial T}{\partial t} + \vec{u} \cdot \nabla T \right) = k_{th,i} \nabla^2 T + Q_{laser} \quad (16)$$

where temperature and time are represented by 'T' and 't', ρ_i denotes the density of the i^{th} phase which. Cp_i and $k_{th,i}$ in Equation 16 the specific heat capacities and thermal conductivities of respective phases, \vec{u} is the flow velocity inside the meltpool. Similarly, Q_{laser} is the heat deposited by the laser following a Gaussian beam profile whose mathematical expression is presented in Equation 17. The temperature dependence of material properties ($\rho_{th,i}$, Cp_i , $k_{th,i}$) are discussed in Section 2.4.

$$Q_{laser} = 1.75 \Omega I \exp \left(-\frac{3r^2}{r_0^2} \right) \quad (17)$$

here 'I' is the laser irradiance (150 kW/cm^2 and 134.6 kW/cm^2), similarly, $\Omega = 6.67 \times \alpha_{Au}$ with the absorption coefficient (α_{Au}) of Au taken as $8.5 \times 10^7 \text{ m}^{-1}$ [5, 69] and a nano-scale laser beam radius r_0 as 120 nm [70]. With the advancement in laser technologies, laser beam with nano-scale precision are being used in practical application such as nano-machining, nano-structuring, nano-ablation, hybrid additive and subtractive processing, crystallization [71, 70, 72]. Here, we have chosen a gaussian beam profile with radius in nano-scale for simplicity of the model describing the phase transition driven by thermal excitation.

2.3. Continuity and Momentum Equations

For the study of fluid flow inside the meltpool regime, the following sets of Incompressible Navier-Stokes equations in Laplacian form (MOOSE Framework's Navier-Stokes Module [73]) are coupled with the phase-field and heat transfer physics. The conservation of mass is given by the continuity equation expressed in Equation 18. Whereas the conservation of momentum is defined by Equation 19 [74].

$$\nabla \cdot \vec{u} = 0 \quad (18)$$

$$\rho_i \frac{\partial \vec{u}}{\partial t} + \rho_i (\vec{u} \cdot \nabla) \vec{u} = -\nabla p + \mu_i \nabla^2 \vec{u} + F_{boussinesq} \quad (19)$$

where, \vec{u} is the flow velocity, ρ_i and μ_i are the density and viscosity of phase i. $F_{boussinesq}$ is given by the Equation 20 for LIQUID phase.

$$F_{boussinesq} = -\rho_i g [1 - \alpha_i (T - T_0)] \quad (20)$$

here Boussinesq effect is observed in only LIQUID phase which is also associated with the convection heat transfer of Equation 16, so $\rho_i = \rho_{LIQ}$ in Equation 20, where α_i is a constant with value -1.44 [5]. As our study primarily focuses on phase transition and IMC grain growth under non-isothermal conditions, we simplify the phase-field model by considering negligible effects of surface tension in meltpool phase.

Table 2

Temperature dependent material properties.

Properties	Expression	Reference
ρ_{LIQ}	$19325.28 - 1.44T + 0T^2$	Bialas et. al. [5]
ρ_{FCC}	$19674.6 - 1.2T + 0T^2$	
ρ_{IMC}	8202.9	Jain et. al [75]
ρ_{HCP}	4504.7	
$k_{th,LIQ}$	$100 + 2.73 \times 10^{-2}T + 0T^2$	Bialas et. al. [5]
$k_{th,FCC}$	$338.9 - 6.93 \times 10^{-2}T + 0T^2$	
$k_{th,IMC}$	91.585	Powell et. al. [76]
$k_{th,HCP}$	16.07	Khvan et. al. [77]
Cp_{LIQ}	$158 + 2.08 \times 10^7 \exp(1.14 \times 10^{-2}T)$	Bialas et. al. [5]
Cp_{FCC}	$132 - 1.1 \times 10^{-2}T + 2.5 \times 10^{-5}T^2$	Chase et. al. [78]
$Cp_{th,IMC}$	428.77	
$Cp_{th,HCP}$	528.049	
M_{LIQ}	$2.908 \times 10^{-15} \exp(-3.043 \times 10^3/RT)$	Luo et. al. [79]
M_{FCC}	$1.741 \times 10^{-15} \exp(7.501 \times 10^3/RT)$	
M_{IMC}	$1.939 \times 10^{-15} \exp(2.15 \times 10^3/RT)$	
M_{HCP}	$1.106 \times 10^{-15} \exp(6.378 \times 10^3/RT)$	
μ_{LIQ}	$\exp(-0.1990 + 2669/T)$	Dubberstein et. al [80]

2.4. Bulk and Interfacial Material Properties

In this section, the material properties associated with individual phases is presented. During the multiple simulations, the LIQUID and FCC phases go through the highest possible temperature fluctuation as a result of direct contact of laser beam at the top surface of the computational domain. Hence, temperature dependent material properties: density, specific heat, thermal conductivity are considered for these two phases whereas for the IMC and HCP phases these properties are taken as a fixed values. The expressions describing the temperature-dependent and constant material properties are presented in Table 2. Whereas the graphs for illustrating the thermal conductivity, density, and specific heat for the FCC and LIQUID phases are shown in Figures 2(a), 2(b) and 2(c), respectively. The temperature dependence of the mobilities for all four phases is considered and expressed as an Arrhenius-type equation presented in Table 2, and are plotted in Figure 2(d). In the Table ‘R’ is the universal gas constant with value 8.3145 J/molK and ‘T’ represents the temperature.

The expression for viscosity of Au-rich LIQUID phase is given by the following expression [80]:

$$\mu_{LIQ} = \exp\left(-0.1990 + \frac{2669}{T}\right) \quad (21)$$

To introduce mushy zone effect, the following Expression 22 is taken into account for viscosity (μ_{adj}) at the LIQUID-FCC boundary region:

$$\mu_{adj} = \psi \times \mu_{LIQ} \times [h_{LIQ} \times h_{FCC}] \quad (22)$$

where ‘ ψ ’ is a constant with value 10 taken for this study. h_{LIQ} and h_{FCC} are the interpolating function for LIQUID phase and FCC phase respectively.

2.5. Initial and Boundary Conditions

The computational domain is set with an initial temperature of 300 K, at normal atmospheric pressure. The initial condition for seven order parameters ($\eta_1, \eta_2, \dots, \eta_7$) is shown in Figure 1(b). The initial compositions of various phases are assigned randomly to numerical values somewhat near to their equilibrium values and during the simulation, the free energy equation will finally ensure that the equilibrium condition is reached. The initial velocity of LIQUID phase η_6 is taken to be 0.

Dirichlet boundary condition is applied at the bottom surface of the domain. In other three sides, the domain is exposed to the ambient air with convection and radiative heat transfer with coefficients λ_{conv} and λ_{rad} expressed in Equation 23.

$$k_{th} \frac{\partial T}{\partial n} = \lambda_{tot}(T - T_{air}) \quad (23)$$

where, $\lambda_{tot} = \lambda_{conv} + \lambda_{rad}$. The convection heat transfer coefficient λ_{conv} of air is taken as $15 \text{ W/m}^2\text{K}$ and the radiation heat transfer coefficient λ_{rad} is expressed as $\lambda_{rad} = \epsilon\theta(T + T_{air})(T^2 + T_{air}^2)$ [81]. The emissivity ϵ of surface is taken as 0.3 and Stefan-Boltzmann constant $\theta = 5.67 \times 10^{-8} \text{ J/sm}^2\text{K}^4$. It is assumed that Au-rich phases (η_6 and η_7) do not mechanically interact with Ti-rich solid η_1 at bottom boundary. Similarly, at top edge, η_1 does not interact with η_6 and η_7 i.e. mathematically,

$$\begin{aligned} \left(\frac{\partial \eta_1}{\partial n} \right)_{top} &= 0 \\ \left(\frac{\partial \eta_6}{\partial n} \right)_{bottom} &= \left(\frac{\partial \eta_7}{\partial n} \right)_{bottom} = 0 \end{aligned} \quad (24)$$

This boundary condition is helpful in suppressing the periodicity effect of microstructures. Natural boundary condition is set for composition variable at all edges. No-slip boundary condition is set for velocity at left, right and bottom edges.

3. Results and Discussion

One of the key parameters that play a crucial role in determining the build quality of a 3D-printed product is the distribution of heat within the specimen undergoing laser treatment.

The heat distribution across the specimen during laser processing plays a crucial role in determining the thermo-physical property of the material being formed. Specially, the amount of deposited heat in the system directly influences the physical phenomena such as melting, solidification, pore and precipitate formation, grain refinement, thermal distortion, and residual stress induction [82]. Additionally, the kinetics of these phenomena namely: convection and diffusion are also affected by the supplied heat. Given the critical impact of heat distribution, this research aims to quantify the resulting physical changes in a computational model by examining two essential laser parameters: laser irradiance and scan speed. To achieve this, we conducted four sets of laser processing simulations on a geometrically identical model, varying the laser irradiance (134.6 kW/cm^2 and 150 kW/cm^2) and scan speed (4 nm/ms and 5 nm/ms).

We further incorporate the thermo-diffusion term into the phase field equations to account for the effects of non-isothermal heating within a finite domain. The presence of a spatial temperature gradient necessitates the incorporation of the term VT/T^2 with the composition ‘c’ in the diffusion term, aligning with approaches demonstrated by Mohanty et al. [83], Kunwar et al. [51] and Oyedeleji et al. [84]. Oyedeleji et al. quantitatively integrate the driving forces for non-isothermal chemical diffusion and thermal diffusion, incorporating the ‘T-c’ cross term. Our model inherits this cross-effect through the terms $B_i(T - T_{eq}^i)^n$ in the equation of Gibbs energy (Equation 4). The presence of this thermal term in the driving force eventually affects the composition distribution in accordance to Equation 9. Moreover, another term $C_i(c_i T)$ in Equation 4 also displays the role of T variable in influencing the composition distribution in the alloy phases. These terms, although in over simplified form, capture the essential physics of phase evolution under thermal gradients. Future work will expand these terms to more accurately represent the physics of thermal diffusion and its impact on concentration gradients in non-isothermal systems.

Using different quantification techniques, such as time-temperature plots, free-energy versus phase stability graphs, and phase diffusion versus thermal diffusion analyses, we aim to elucidate the correlation between these laser parameters and the resulting microstructural changes. These changes include intermetallic grain growth, melt pool dynamics (depth, width, and area), heat-affected zone stability, and overall microstructural evolution within the domain. These findings are discussed in detail in the following sections.

3.1. Scan-Speed’s Influence on Thermal History

To understand the effects of variations in laser scan speed within the computational domain, we conducted simulations while keeping all other model parameters identical. We ran two simulations with scan speeds of 4 nm/ms and 5 nm/ms. Figure 3 shows the temperature distribution across the computational domain when a laser with a power

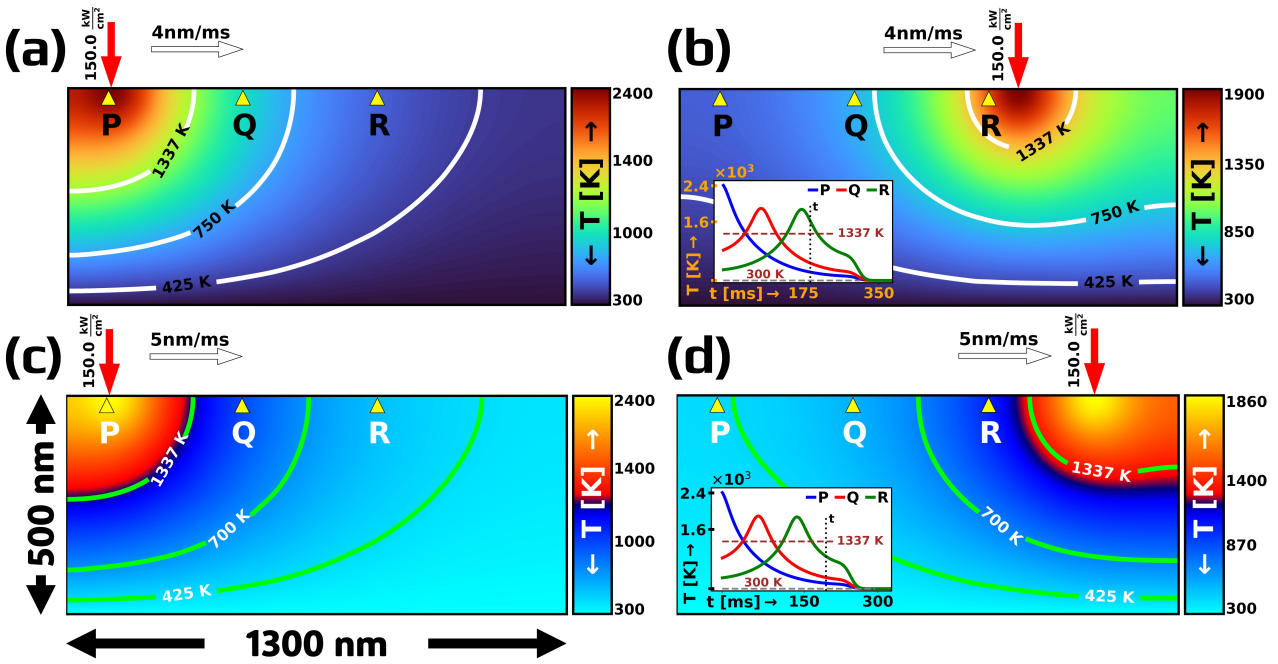


Figure 3: Illustration of a composite set of four snapshots from phase-field laser simulations conducted on a $1300\text{ nm} \times 500\text{ nm}$ computational domain, subjected to a laser irradiance of 150 kW/cm^2 at varying scan speeds of 4 and 5 nm/ms. The two images on top half depict snapshots from the same simulation with a scan speed of 4 nm/ms at two distinct time points: (a) $t = 1.2\text{ ms}$ and (b) $t = 190\text{ ms}$, respectively. In (a), the initial laser application results in a rapid temperature surge, peaking at approximately 2400 K, with a discernible temperature gradient away from the laser impact point. Figure (b) illustrates the temperature distribution after 190 ms of laser exposure, reaching a horizontal distance of 885 nm from the left edge. The temperature distribution averages out, peaking at 1900 K directly beneath the laser source. A time-temperature plot inset provides a temporal profile for three spatial points (P, Q, and R) on the system's top surface, each separated by 350 nm. The plot further indicates a total simulation duration of about 350 ms for these selected points to cool down to ambient temperature post-laser treatment. Similarly, bottom two images showcase snapshots from a different simulation with a faster scan speed of 5 nm/ms. Initially, at (c) $t=1.2\text{ ms}$, the effects of the higher scan speed are indistinguishable, with a maximum temperature reaching a similar range of 2400 K at the beam focus. However, at (d) 190 ms (equivalent to (b)), the impact of the higher scan speed becomes evident. The laser covered a greater distance of 1075 nm from the top left edge, and the maximum temperature at the laser illumination center is lower (1860 K) compared to the slower scan speed. This is attributed to the shorter laser exposure time due to the faster scan speed, resulting in less heat deposition into the specimen. The inset time-temperature plot within image (d) illustrates that the laser's overall traversal time for points P, Q, and R, with substantial cooldown to ambient temperature, is comparatively shorter (below 300 ms) than in previous case with a slower scan speed.

density of 150 kW/cm^2 is applied at two distinct scan speeds: 4 nm/ms in (a) and (b), and 5 nm/ms in (c) and (d). To quantify the effects of laser scan speed, we selected two simulation instances at different time steps: one at the beginning of the laser treatment ($t = 1.2\text{ ms}$) and another at 190 ms into the simulation. Figures 3(a) and (c) represent the simulation snapshot at $t = 1.2\text{ ms}$, while (b) and (d) correspond to $t = 190\text{ ms}$, respectively.

Initially, the effect of increased laser scan speed from 4 nm/ms to 5 nm/ms is not distinctly visible at the beginning. For both conditions, the maximum temperature attained by the domain was 2400 K, as illustrated in Figures 3(a) and (c). Similarly, the temperature gradient away from the laser beam spot (in both axes) is practically indistinguishable, as denoted by the temperature contour lines. This may be due to the fact that initially, the entire domain is at 300 K, and the heat energy from the laser incident on the left-top surface takes some time to diffuse throughout the computational domain, which cannot be fully captured within 1.2 ms. To observe and evaluate the actual effects caused by the difference in scan speed, we examined the temperature distribution at a later time step. Figures 3(b)

and **(d)** demonstrate the simulation snapshot at $t = 190$ ms, where the consequences of different laser speeds are more apparent. The first observable difference is the laser position; in **(d)**, with a higher scan speed, the laser traversed a greater distance from the left-top of the domain compared to **(b)**. The inset plots in Figures 3**(b)** and **(d)** show the time-temperature graphs for three randomly selected spots at the top surface (P, Q, and R) inside the computational model. These plots indicate that the total simulation time required for the selected points to heat up and subsequently cool down to ambient temperature is longer (350 ms) for the slower scan speed compared to the faster one (300 ms). Since the laser irradiance is the same in both cases, the heat flux is higher for the lower speed than for the higher speed. This means the heat energy is imparted for a longer time at the point of beam incidence, consequently increasing the temperature of the domain. This phenomenon is observed in Figure 3**(b)**, where the maximum temperature attained by the system is 1900 K, whereas at the same simulation time of $t = 190$ ms, in **(d)**, the system peaked at 1860 K. The detailed simulation videos depicting the thermal history for two different scan speeds and two irradiance levels is available in the Supplementary Section A. Videos A1, A2, A3, and A4 illustrate the temperature distribution across the simulation domain as the laser moves from left to right on the top surface, with scan speeds of 5 nm/ms and 4 nm/ms, and irradiance levels of 150 kW/cm^2 and 134.6 kW/cm^2 , with all the combinations of these parameters respectively.

3.2. Effects of Power Density

Next, we discuss about the effects of the most critical laser processing parameter: irradiance or power-density [85, 44] by exploring its impact on the computational model through a comparative study of laser irradiance at two levels: 150 kW/cm^2 and 134.6 kW/cm^2 . Figure 4**(a)** presents the time-temperature plot corresponding to three selected spots at the domain's top surface (P, Q, and R as shown in the inset picture) obtained from two separate simulations with different laser irradiance levels at a constant scan speed of 5 nm/ms. The solid lines represent points irradiated by a laser with 150 kW/cm^2 , while the dotted lines represent points irradiated by a laser with 134.6 kW/cm^2 .

The most noticeable differences between the time-temperature plots for the two laser irradiance levels are in: (i) The peak temperature attained by the computational domain, and (ii) The duration for which the selected points stay above the thermal melting zone (>1337 K). It is evident that a higher temperature is attained by the simulated domain when irradiated by a laser with higher irradiance. As confirmed by Figure 4**(a)**, all solid lines are above the dotted lines on the temperature scale. However, this increase in temperature has further impacts on the system that pose a greater challenge to quantify during actual laser experiments specifically, the duration for which any given point in the system remains above the thermal melting zone. Using post-processing tools in Python, we measured the total time during which the three selected points (P, Q, and R) remain above the theoretical melting temperature of gold (1337 K) as the laser traverses through these points. The measurement results indicate a similar trend to that of peak temperature: with higher laser irradiance, these points remain above the thermal melting zone for a longer duration (Q: 55 ms, R: 53 ms) compared to lower laser irradiance (Q: 42 ms, R: 41 ms).

While Figure 4**(a)** visualizes the time-temperature profile at three specific points on the domain, Figures 4**(b)** and **(c)** present the distribution of temperature at time $t = 100$ ms for two levels of laser irradiance: 134.6 kW/cm^2 and 150 kW/cm^2 , respectively. At a constant scan speed of 5 nm/ms, the horizontal distance traversed by the laser is the same in both cases. Comparing the two snapshots, **(b)** and **(c)**, we can readily identify several key differences in temperature profiles between them. Firstly, the peak temperatures are 1650 K (for 134.5 kW/cm^2) and 1860 K (for 150 kW/cm^2). Secondly, the area of the domain lying inside the thermal melting zone of 1337 K is greater for the higher laser power than the lower one. This can be visually verified by the contour line of 1337 K covering a deeper and wider field (nearly touching point Q and P) in **(c)** than in **(b)**. Similarly, the contour line for 700 K touches point P in **(c)**, covering a larger area compared to **(b)** with lower laser irradiance.

Similarly, the effect of laser irradiance can be observed within the meltpool, where the flow velocity of the LIQUID phase is higher for high power density and lower for low power density. Figure 5 illustrates the convective flow inside the meltpool at two levels of irradiance: **(a)** shows the flow characteristics for 150 kW/cm^2 , and **(b)** for 134.6 kW/cm^2 . The figure compares the maximum flow velocity in the LIQUID phase at a constant scan speed of 5 nm/ms, 144 ms into the simulation. For high laser irradiance, the maximum flow velocity inside the meltpool is nearly twice that for low irradiance. This demonstrates that not only are the size and shape of the meltpool directly associated with laser intensity, but the convective flow and its maximum magnitude inside the meltpool are also closely linked with laser power density.

With the consideration of temperature dependent free energy formulation we present a more realistic representation of temperature distribution across the meltpool and solid phases. Unlike other works [54, 49], where the thermal profile coupled with the phase field is taken at just two fixed temperature values, as shown in Figure 6**(a)**, we present

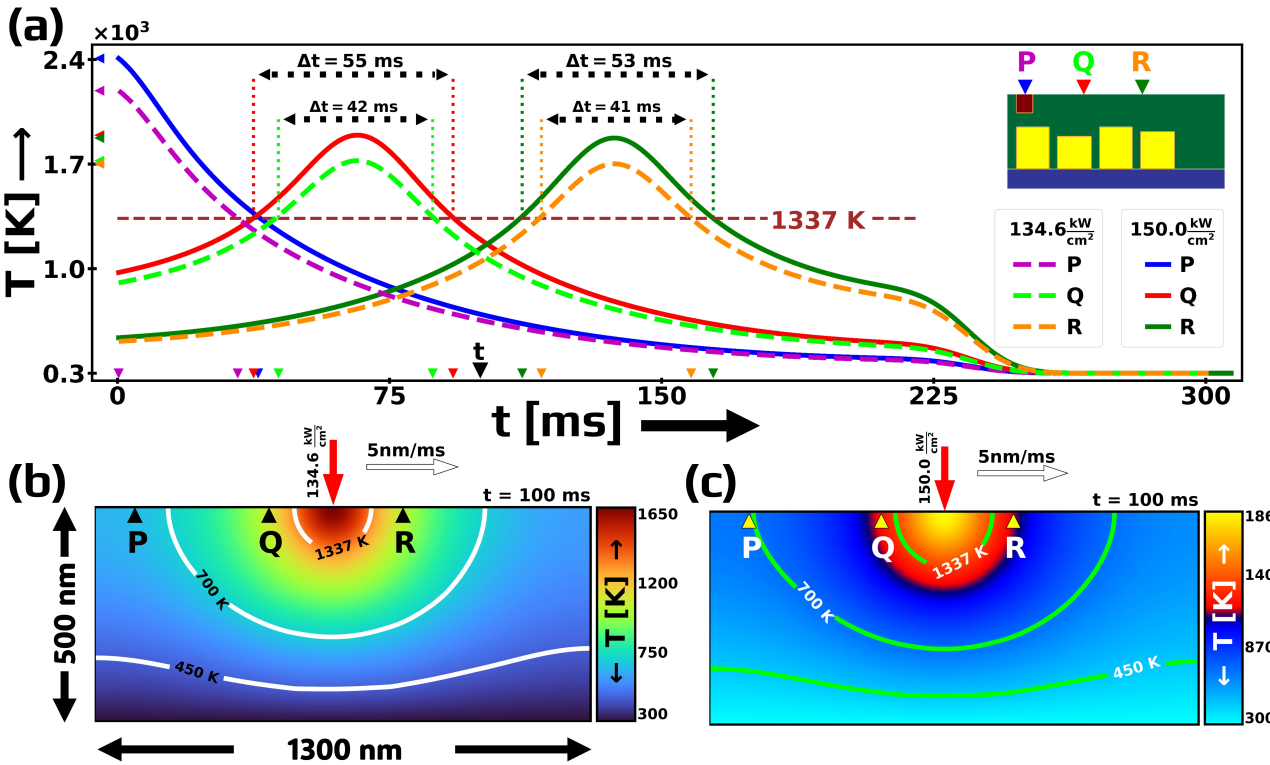


Figure 4: Laser irradiance's effects on T profiles. (a) Plot illustrating the temporal temperature distribution at three specific spatial coordinates (P, Q, and R, as indicated in inset figure) located on the top ($z=500\text{nm}$) at $x=105, 455$ and 805 nm respectively for two distinct irradiance levels. The continuous blue, red, and green lines represents the temperature variations at points P, Q, and R, under laser irradiance of $150\text{ kW}/\text{cm}^2$ and a speed of $5\text{ nm}/\text{ms}$. Conversely, the dashed magenta, light green, and orange lines represents the temperature profiles at the same points under $134.6\text{ kW}/\text{cm}^2$ irradiance at the identical speed. Notably, at higher laser irradiance, all three location points remain above the melting temperature (1337 K) for a significantly longer duration: 38.75 ms , 55 ms , and 53 ms compared to the lower irradiance scenario where the same coordinates experience above melting temperatures only for 33.12 ms , 42 ms , and 41 ms , respectively. The graph emphasizes that not only does higher irradiance guarantee longer peak T in the material, but it also significantly alters the temporal status of the thermal melting zone, even at the exact same scan speed. (b) Snapshot of the temperature field distribution profile captured at 100 ms (during midway), employing an irradiance of $134.6\text{ kW}/\text{cm}^2$ and a scan speed of $5\text{ nm}/\text{ms}$. Notably, the computational domain reaches a maximum temperature of 1650 K at the laser impact point on the surface. Contour lines delineate three distinct temperature regimes at 450 K , 700 K , and the FCC melting point of 1337 K . Similarly, in (c), the temperature distribution at the same time point ($t=100\text{ ms}$) is visualized, maintaining the identical laser scan velocity but with a higher irradiance of $150\text{ kW}/\text{cm}^2$. A visually distinctive feature is the extended region surpassing the melting point, with a general maximum temperature of 1860 K recorded at the laser-irradiated surface spot. Collectively, images (a), (b), and (c) intricately convey that the overall dynamics of heat transfer and melting point regime exhibit significant variation with laser power, even when the scanning speed is held constant.

a fully coupled continuous temperature-phase-field system, allowing the temperature to vary according to the heat deposition by a Gaussian beam profile. The issue with considering a constant temperature within a phase in above mentioned studies is the lack of continuously differentiable free energy function dependent on temperature, which is primarily responsible in dictating the phase transitions. Hence, to interpolate phase field variables and associated material properties within phases, a fixed reference temperature is used in those studies. This assumption undermines the realistic representation of laser processing, as illustrated by the top-hat curves for phase (ϕ : sky blue line) and temperature (red line) in Figure 6(a), where it is observed that the phase changes occur instantaneously as the temperature shifts. In contrast, the formulation of a continuous function of temperature-dependent free energy in our

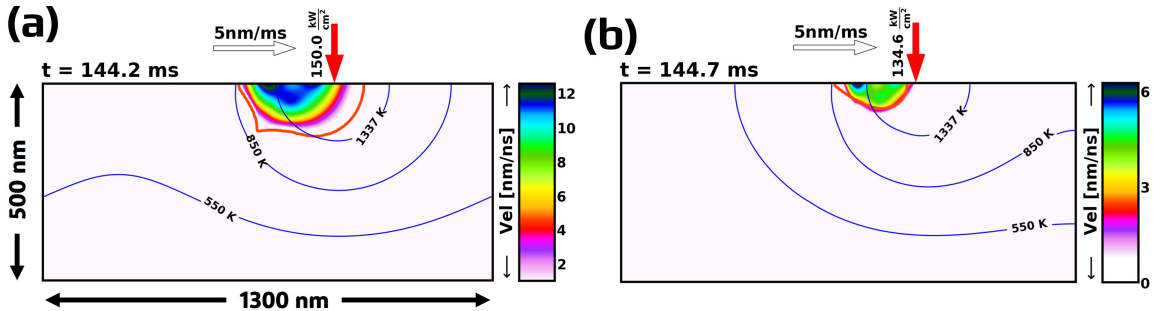


Figure 5: Illustration of the effect of laser irradiance on convective flow inside the melt pool regime. (a) Shows the magnitude of flow velocity inside the liquid phase (marked by the orange contour line) for laser irradiance of $150 \text{ kW}/\text{cm}^2$. The maximum velocity magnitude is observed at the top surface of the domain with a value greater than 12 nm/ns , decreasing gradually with depth, and reaching zero outside the liquid phase. (b) depicts the convective flow velocity inside the melt pool for irradiance of $134.6 \text{ kW}/\text{cm}^2$. It is to be noted that the maximum velocity magnitude is nearly half (6 nm/ns) that of (a). The scan speed for both simulations was set to 5 nm/ms , and the velocity profile snapshot is taken at 144 ms into the simulation.

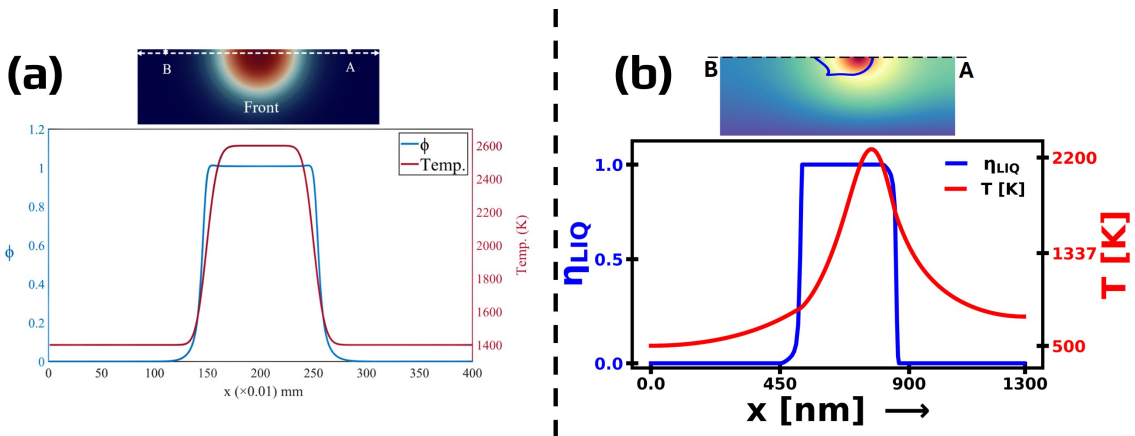


Figure 6: Comparison of temperature distribution across the liquid (melt pool) and solid phases between the work of Darabi et al. [54] (a), which uses a constant temperature interpolation between phases, and our work (b), which employs a temperature-dependent free energy functional and material properties. (a) Plot of phase field and temperature variation graph along the A-B line in the melt pool boundary domain [54]. A fixed two-temperature model is illustrated by the uniform temperature of 2600 K across the entire melt pool regime ($\phi = 1$), displaying a top-hat profile, and a temperature of 1400 K in the solidified region ($\phi = 0$). (b) The phase field plot for the liquid phase and the temperature profile along the A-B line from our work. The bell-shaped temperature distribution demonstrates a smooth and continuous temperature profile across the melt pool. The spatial lead of the temperature profile relative to the liquid phase is due to differences in thermal and phase diffusion rates.

work allows us not only to observe differences in thermal and phase diffusion but also to achieve a realistic temperature distribution (Gaussian profiled red line) and phase profile (blue line), as shown in Figure 6(b).

From these graphs of time-temperature, temperature distribution in Figures 4, 6 and convective flow of Figure 5, we can leverage laser irradiance for a tailored design approach to control the area of the heat-affected zone (HAZ), thermal melting zone, flow characteristics inside melt pool, as well as the time period for melting-solidification of any given spatial area of the domain.

3.3. Phase Dynamics

With different laser parameters, we observed a different nature of microstructural growth of each phases. In the Figure 7, each yellow block indicates the Ti_3Au IMC grain marked as G_1 , G_2 , G_3 , and G_4 , the melt pool region is

represented by dark red color with Au-rich FCC phase in green. The Ti-rich HCP phase is shown in blue, and the dotted contour lines inside the domain denotes the temperature distribution. The result from four different sets of simulation criteria are presented inside the dotted blocks with upper rectangular block representing phase evolution under laser power of 134.6 kW/cm^2 , and the one in bottom corresponding to that of 150 kW/cm^2 . Inside of each block, the first row corresponds to scan-speed of 5 nm/ms and second row to 4 nm/ms . To analyse the temporal evolution of Ti_3Au intermetallics, snapshot of the domain at two time stamps are presented in columns: **(a)** at $t = 40 \text{ ms}$ and **(b)** at $t = 200 \text{ ms}$.

Analysing the results from four simulations setup, it was found that IMC grain growth is largely enhanced by a higher value of irradiance at slower scan-speed. It can be observed that under the influence of maximum heat flux condition (\dot{Q}_{max}) the overall growth of all the 4 grains is highest and in minimum flux condition (\dot{Q}_{min}) the grain growth is not so prevalent. The maximum and minimum heat flux conditions are defined as a set of combination of laser irradiance and scan speed, for \dot{Q}_{max} the irradiance is 150 kW/cm^2 with scan-speed 4 nm/ms and for \dot{Q}_{min} , the irradiance is 136.4 kW/cm^2 at a faster scan-speed of 5 nm/ms .

From the post-simulation calculation, for \dot{Q}_{min} (topmost row) the area of melt pool is computed to be $48.05 \times 10^3 \text{ nm}^2$ at $t = 40 \text{ ms}$ and $21.60 \times 10^3 \text{ nm}^2$ at $t = 200 \text{ ms}$, the lowest in all four simulation results. In the second row of Figure 7, with a slower scan speed of 4 nm/ms , the heat deposition increases compared to the \dot{Q}_{min} condition. The melt pool area measures $54.44 \times 10^3 \text{ nm}^2$ at $t = 40 \text{ ms}$ and $36.55 \times 10^3 \text{ nm}^2$ at $t = 200 \text{ ms}$. For the IMC grains, particularly grain G_1 is observed to be protruding further downward at the later time stamp. In the third row, with a higher laser irradiance of 150 kW/cm^2 , the grains G_1 and G_2 start to grow and come in contact with each other at time $t = 40 \text{ ms}$ which indicates a preferential growth of IMC at an elevated temperature (800 K). This growth is attributed to the lower Gibbs free energy (-12.532 kJ/mol) and higher mobility ($14.03 \times 10^{-16} \text{ m}^5/\text{Js}$) of IMC compared to near FCC phase with free energy -8.49 kJ/mol and phase mobility of $5.63 \times 10^{-16} \text{ m}^5/\text{Js}$ at 800 K . At $t = 200 \text{ ms}$, not only do all IMC grains evolve rapidly, but the melt pool area also increases to $39.26 \times 10^3 \text{ nm}^2$ compared to that with irradiance of 134.6 kW/cm^2 at same scan-speed.

In the fourth row, an extreme phase morphology is observed throughout the simulation. The area of melt pool dominates all other phases with an area of $125.56 \times 10^3 \text{ nm}^2$ at time $t = 200 \text{ ms}$. Evolution of all the IMC grains is observed through the consumption of nearby FCC and HCP-rich regions. This particular snapshot of the simulation at \dot{Q}_{max} condition also highlights an intriguing phenomenon where phase diffusion lags behind thermal diffusion, which is discussed further in Section 3.7.

3.4. Area Evolution

Further quantification of individual phase growth in response to changes in laser parameters are discussed within this section primarily focusing on the growth and shrinkage of phase areas. With an area-time plot for two extreme cases of maximum (\dot{Q}_{max}) and minimum (\dot{Q}_{min}) heat flux Figure 8 demonstrates the temporal growth of all the phases. Figure 8(a), corresponding to \dot{Q}_{min} with an initial dominance of the Au-rich FCC phase (green line) undergoing transitions with an area of $3.45 \times 10^5 \text{ nm}^2$ at $t = 0 \text{ ms}$. As the laser irradiates the top surface of the domain, solid FCC melts to form LIQUID phase represented by red line peaking its area from $0.1 \times 10^5 \text{ nm}^2$ initially to $0.51 \times 10^5 \text{ nm}^2$ at $t = 53 \text{ ms}$. As the laser progresses through the domain, noteworthy growth in IMC grains is observed (yellow line) at $t = 150 \text{ ms}$ around mid-simulation. By 225 ms into the simulation, FCC phase reduces to its minimum with area of $2.65 \times 10^5 \text{ nm}^2$, while the melt pool re-expands to $0.41 \times 10^5 \text{ nm}^2$. During the end of the simulation ($t = 300 \text{ ms}$), the melt pool solidifies back into the FCC phase, augmenting the Au-rich phase. Meanwhile, the IMC grains expansion slowly plateaus. For the HCP phase (blue line), its initial area of $1.3 \times 10^5 \text{ nm}^2$, reduces to $0.74 \times 10^5 \text{ nm}^2$ at $t = 150 \text{ ms}$, and by the end at $t = 281 \text{ ms}$ it further drops to $0.29 \times 10^5 \text{ nm}^2$.

Similarly, in plot 8(b) the area-time profile under maximum heat flux conditions (\dot{Q}_{max}) is presented. Although the initial phase areas are identical to \dot{Q}_{min} condition, a drastic difference in phase growth is observed. Starting with the FCC to LIQUID phase transition due to laser-induced melting, the Au-rich FCC phase undergoes a conspicuous 'U'-shaped dip in the area curve, reaching its all-time low presence of $0.9 \times 10^5 \text{ nm}^2$ at $t = 275 \text{ ms}$. At the same time, the melt pool area takes a sharp ascent, with a maximum area of $1.57 \times 10^5 \text{ nm}^2$. Implying that higher laser power coupled with a slower scan speed exerts a more profound influence on phase morphologies compared to lower irradiation with a faster scan speed. After 275 ms , as the laser traverses fully through the domain, the melt pool solidifies decreasing its area from $0.39 \times 10^5 \text{ nm}^2$ at 500 ms to near non-existent by the end with an increase in FCC phase area to $2.4 \times 10^5 \text{ nm}^2$. Concurrently, the cumulative area of Ti_3Au IMC grains peaks to $38.06 \times 10^5 \text{ nm}^2$ at $t = 275 \text{ ms}$ and remains

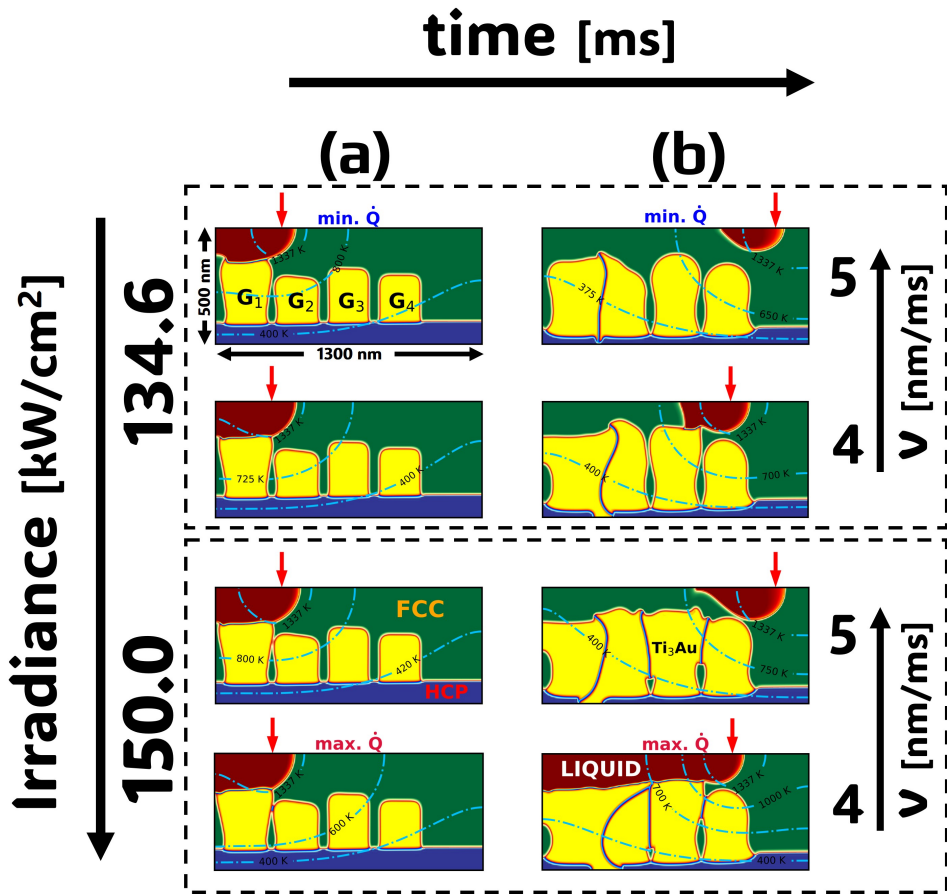


Figure 7: Utilizing phase field simulations to explore the combined effects of irradiance and scan speed on phases/grain sizes and morphologies during transient heating process. For minimal boundary heat flux rate (\dot{Q}) condition (indicated by process parameters of 134.6 kW/cm^2 , 5 nm/ms on the topmost images), the yellow colored IMC grains G_1 , G_2 , G_3 and G_4 of size and morphology quantified at (a) $t = 40 \text{ ms}$, evolve to the nanostructures of different profile and dimensions at (b) $t = 200 \text{ ms}$. Among the four grains, the grain G_1 being the first one to meet the melt pool since 40 ms takes the opportunity to not only become the largest and widest at 200 ms . When the \dot{Q} is increased with only the decrease of scan speed at same irradiance (corresponding to 134.6 kW/cm^2 , 4 nm/ms), it allows G_1 to expand laterally + vertically even bigger at the cost of adjacent phases and grains, thereby suggesting that the IMC grains appearing first to the slowly travelling heat source benefit the most at the fixed time duration of $200 - 40 = 160.0 \text{ ms}$. However, when irradiance is increased to 150.0 kW/cm^2 with scan speed maintained higher at 5 nm/ms , the grains G_2 , G_3 and G_4 compete proportionately with G_1 for growth. Finally, as in the context of images in the bottommost part of the figure, when the maximal \dot{Q} criterion is implemented (150.0 kW/cm^2 , 4 nm/ms), the slowly moving and high powered laser beam again favors G_1 grain the most. Observing the melt pool profiles (red colored LIQUID phase) corresponding to 200 ms , the one for minimal \dot{Q} condition is the smallest and touches none of the IMC grains, whereas the melt pool of maximal \dot{Q} criterion is the largest, the longest and completely touches the three grains G_1 , G_2 and G_3 . It is to be noted that meltpool front for 5 nm/ms speed are ahead than those for 4 nm/ms . Comparing between the images at 200 ms , the FCC phase (green colored region) and HCP substrate (blue colored region) retain the largest areas for minimal \dot{Q} criterion and the smallest areas for maximal \dot{Q} condition.

relatively constant till the end. Meanwhile for HCP phase, a sharp decrease in area is observed initially reducing to $0.21 \times 10^5 \text{ nm}^2$, and after $t = 275 \text{ ms}$ it almost maintains constant area.

The simulation videos displaying phase evolution through animated area graphs are provided in the Supplementary Section A. Videos A5, A6, A7, and A8 illustrate the growth and area evolution of individual phases. These videos

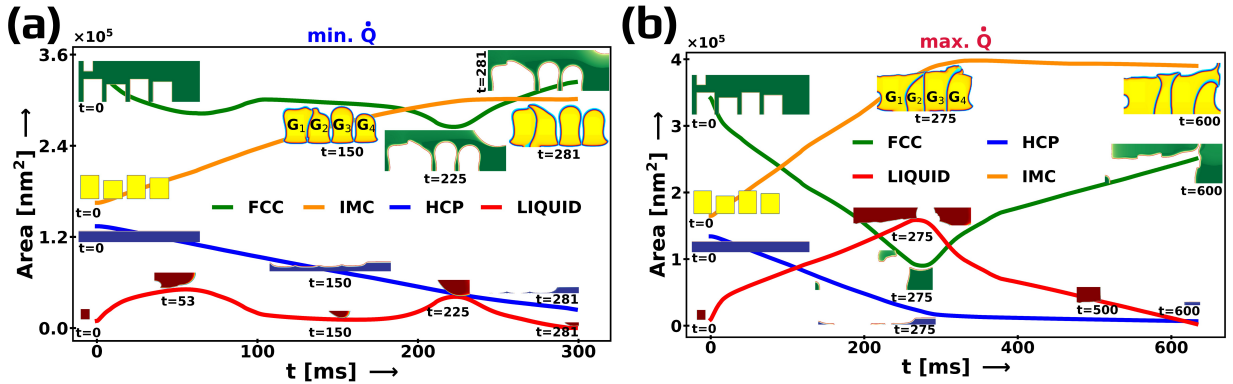


Figure 8: Synopsis of temporal variation of the individual areas for LIQUID, FCC, IMC, and HCP phases for two conditions of boundary heat source - (a) \dot{Q}_{min} (134.6 kW/cm^2 , 5 nm/ms), and (b) \dot{Q}_{max} (150.0 kW/cm^2 , 4 nm/ms). The phase area of IMC is quantified as the total areas of the four grains G_1 , G_2 , G_3 and G_4 . The time taken by the laser for (b) to reach the another end of the computational domain from the start position is twice that of (a). At the time the laser finishes its journey, the IMC phase (orange colored lines) acquires the largest area in context of (b) \dot{Q}_{max} criterion whereas FCC (green colored lines) retains its initial position in case of (a) \dot{Q}_{min} criteria. Since LIQUID (red colored lines) and FCC phase replace each other during melting and resolidification, the increase in area of one of the two phases is marked by the decrease in the size of the another phase. In context of \dot{Q}_{min} condition, the FCC phase area is always larger than the LIQUID area throughout the entire path of the laser, and with a difference of at least $2.138 \times 10^5 \text{ nm}^2$. In \dot{Q}_{max} condition, the difference of area is reduced as time passes till the meltpool (LIQUID phase) area temporarily exceeds that of the FCC area for a duration of 91.09 ms midway. Again the FCC phase area surpasses the LIQUID area till the end. The HCP phase being consumed by the growing IMC grains, keeps on ceding its area in both conditions but the loss rate is more pronounced in context of maximal heat source application criterion.

correspond to the laser scan speeds of 5 nm/ms and 4 nm/ms , with irradiance levels of 150 kW/cm^2 and 134.6 kW/cm^2 , respectively, representing all combinations of these parameters.

From a broader observation of simulation results in Figures 7(a) (b) and 8(a) (b), it can be noted that the area of intermetallic grains (Ti_3Au) grows with an increase in temperature of the simulation domain which is consistent with the two different experimental works from Karimi et al. and Lukose et al. [13, 12]. The increase in temperature of the computational domain corresponds to a higher laser irradiance and a slow scan speed. Our numerical simulation is in agreement with these experimental observations that the increase in power input accelerates the morphological appearance of conspicuously columnar intermetallic grains.

3.5. Laser Meltpool Characteristics

Understanding laser-induced meltpool characteristics such as shape, depth, width, and temperature is crucial in advancing the quality and efficacy of laser-based additive manufacturing processes [86]. Meltpool geometry and area are two highly influential factors determining the microstructure, along with the kinematics of solidification, cooling rate, phase transition and dendrite growth [87]. Tracking the interface via the phase field method, we measured the ever-changing dynamics of the LIQUID phase: the temporal evolution of the maximum width (x_{max}) and the changes in meltpool maximum depth (z_{max}). In addition, a comparative analysis of the time-temperature profile and free energy changes of the heat affected zone (HAZ) with that of meltpool region is done by selecting two study points (\circ and \times , as marked in the inset of Figure 9(a)). These two selected points are 10 nm from the interface on either direction with each lying inside HAZ (FCC phase) and meltpool (LIQUID phase) at a fixed distance from the top surface. As, these points are linked to the FCC-LIQUID interface, their absolute coordinates inside the domain vary as the interface moves along the domain.

In Figure 9(a), the four subplots illustrate the changes in Gibbs free energy over time at \circ and \times with different laser parameter setup. A horizontal black dotted line is used to demarcate the zero free energy value, separating positive (unstable) and negative (stable) realms. Considering the tendency of reactions to minimize free energy for maximum stability, observing the temporal evolution of free energy graphs provides an insight into the phase stability

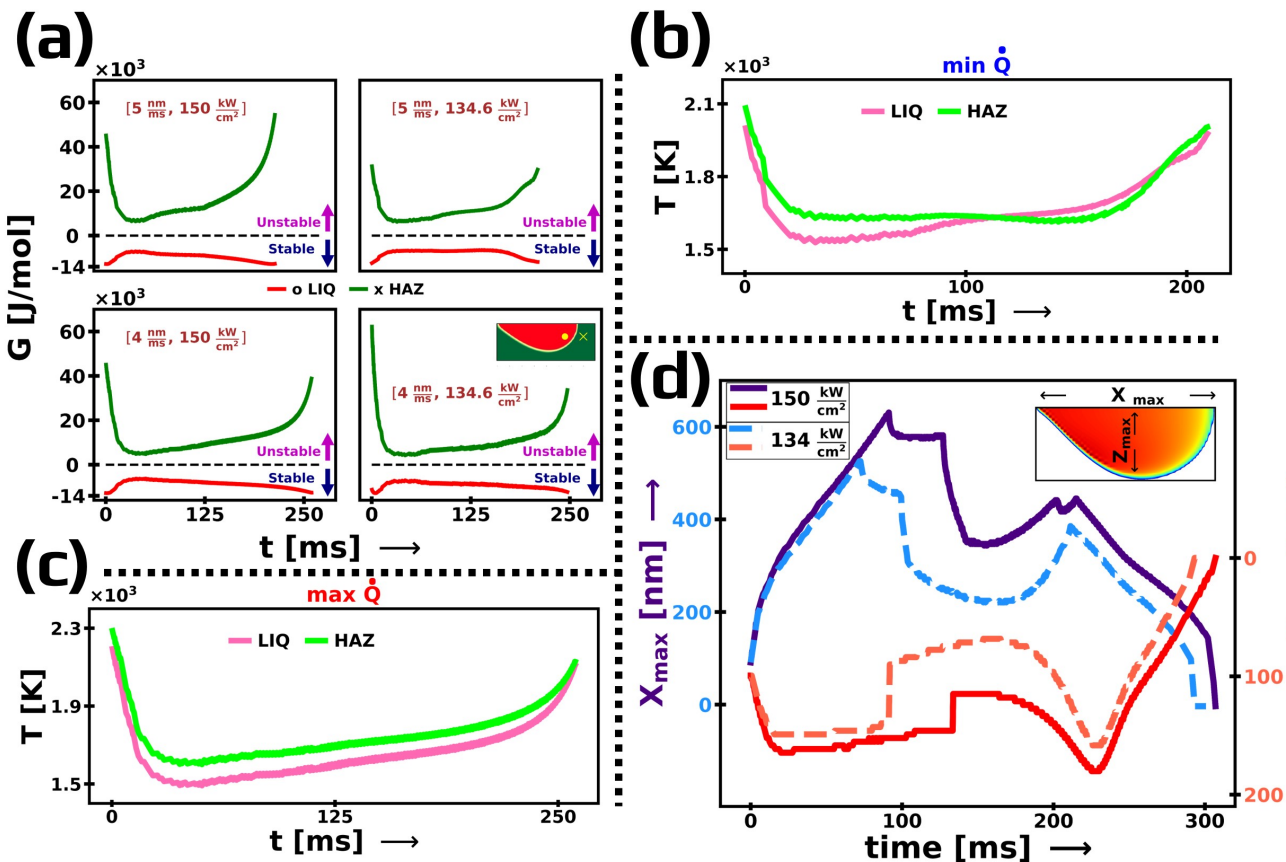


Figure 9: Assessment of thermodynamic stability of melt pool is performed in (a)-(c). The images in (a) demonstrate how laser irradiance and scan speed influences free energy profiles at the forefront of an advancing melt pool. The red colored free energy curves representing the position dot (o) located within the LIQUID phase of the meltpool 10 nm inward from the phase interface are negative throughout the entire time duration. On the other hand, the cross (X) position located at the solid FCC phase 10 nm outward from the phase interface, has a positive valued F values through out the entire duration and thus indicates that it will be consumed by the advancing melt pool (relative position of dot 'o' and cross 'x' is presented in the inset figure of (a)). The temperature values that dictate the F values for the two locations - one positioned at the LIQUID phase (LIQ) and another at heat affected zone (HAZ) of FCC phase, are plotted as functions of time for processing parameters of (b) 150 kW/cm^2 , 4 nm/ms (max Q) and (c) 134.6 kW/cm^2 , 5 nm/ms (min Q) criteria. The graph in (d) reveals how the transient melt pool size (characterized geometrically by horizontal span x_{\max} and vertical depth z_{\max}) is increased two-dimensionally by the amount of the irradiance values of a boundary heat source moving at a constant speed of 5 nm/ms . The magnitudes of x_{\max} and z_{\max} are differentiated through the colors of the labels in the vertical axes. The lengths (span and depth) for higher irradiance value of 150 kW/cm^2 are represented by solid lines whereas those for lower irradiance (134.6 kW/cm^2) are depicted by dotted lines. For applied irradiance of 150 kW/cm^2 , the meltpool span achieves its peak value of 630.72 nm at 91 ms whereas the largest depth of 180.12 nm at 225 ms .

of these points. Notably, in all four subplots of (a), the free energy at the HAZ point marked by 'x' is persistently large and positive, indicating its pronounced instability. In contrast, the point 'o' within the LIQUID phase consistently demonstrates significantly negative free energy, signifying stability. Thus, it can be inferred that as the laser advances, the phase at the HAZ proceeds to transition towards a more stable LIQUID phase. In Figures (b) and (c), the time-temperature plots illustrate the thermal responses at two selected points under \dot{Q}_{\min} and \dot{Q}_{\max} conditions. As these points traverse along with the FCC-LIQUID interface during the simulation, observable temperature fluctuations manifest. Notably, both coordinates (o and x) consistently register temperatures well above the FCC melting point,

signalling an impending phase transition from the heat-affected zone to the LIQUID phase. The temperature-time diagrams between \dot{Q}_{min} and \dot{Q}_{max} conditions for these two points shows a observable difference in peak temperatures attained, with temperatures reaching approximately 2100K for \dot{Q}_{min} and around 2300K for \dot{Q}_{max} . Additionally, the curves representing \dot{Q}_{max} exhibits higher temperature for region of interest inside heat-affected zone compared to that inside LIQUID phase. Conversely, for \dot{Q}_{min} conditions, a fluctuating competition emerges between point of interest inside the HAZ and that inside the LIQUID phase to achieving a higher temperatures.

The free energy and temperature evolution of the region around the FCC-LIQUID interface provide an essential insight into the potential development of the LIQUID phase during laser processing. To characterize the actual meltpool formed due to laser melting of the FCC-rich phase, we traced the maximum meltpool width and depth throughout the simulation at two laser irradiance levels (134.6 kW/cm² and 150 kW/cm²) for same scan-speed of 5 nm/ms. We found that the relationship between x_{max} and z_{max} with the laser irradiance level is straightforward: the higher the irradiance, the greater the width and depth of the meltpool, aligning with the study by Li, et. al. [88].

As shown in Figure 9(d), the maximum meltpool depth consistently surpasses at each time instance for higher laser power (red solid line), with a maximum depth of 180.12 nm at $t = 225$ ms, at the same time the dotted red line represents the lower irradiance level with a maximum depth of 158.3 nm. The meltpool width mimics the meltpool depth, i.e. higher laser irradiance yields larger x_{max} values at each time step (purple solid line peaking at 630.72 nm at $t = 91$ ms). In contrast, the x_{max} values for the lower irradiance of 134.6 kW/cm² peak at 72 ms in the simulation, registering a value of 525.6 nm, represented by the dashed light blue line. One key noticeable distinction between the curves of x_{max} for the two irradiance levels is the sharp decrease in meltpool width for higher irradiance (solid purple line) from $t = 127$ ms to $t = 143$ ms, which can be attributed to the separation of the meltpool at the trailing edge as a result of rapid solidification, while the leading front follows the laser. (The videos of these simulations analysis are provided as supplementary material and is also available at https://github.com/subediupadeth/MultiPhysics_MultiPhaseField_LaserProcessing/tree/main/3_Simulation_Video_Animations).

3.6. Interdiffusion and IMC Growth

One common theme that was observed in all four simulations performed with different laser processing parameters was the growth of Ti₃Au intermetallic grains. To understand the thermodynamic reason behind the observable grain growth, we need to focus on the interfacial region between IMC phase and other phases in contact. The non-isothermal conditions in the domain creates an unique effect on the driving force and evolving phases. To study the detail intricacies ongoing in the interfacial region, we proceed to calculate the free energy's numerical value at IMC interface and analyse the behaviour of evolution with regards to free energy value. For this, a point in interface is selected for each IMC grain as marked by 'x' in the inset of Figure 10(d). These marked points are dynamic in nature and shift their position as interface itself moves to minimize the free energy of the system.

In Figure 10, the temporal changes in free energy values at the upper interface of IMC grains is presented. Figure 10(a) showcases \dot{Q}_{min} condition where consistently the lowest free energy value is calculated at the interface for all four IMC grains (yellow lines) implying the continuous growth of Ti₃Au intermetallics. Additionally, from the same graph it can deduced that there is only one grain G₁ interacting with the meltpool marked by the presence of red solid line in plot for G₁ and absence in all others. The interaction between IMC and grain G₁ is very brief lasting only for 21.8 ms after which, the only interaction of IMC grains is with FCC phase (green line). Throughout the simulation, the free energies of interacting phases IMC grains and FCC is always minimum for IMC giving rise to its eventual growth. Similarly, for \dot{Q}_{max} condition, the plot is presented in Figure 10(b) where a distinct phenomenon is observed for grain G₁ and G₃. For grain G₁, at the beginning of simulation the LIQUID phase dominates the interfacial region resulting in meltpool area increase. After 22.67 ms into the simulation, the driving free energy at interface region shifts from LIQUID phase to IMC and hence IMC grain G₁ grows. For grain G₃, the IMC interface comes into contact with meltpool mid-simulation (from 125.31 ms to 147.48 ms) elsewhere the phase in contact is FCC. Although the interface contact changes from FCC to LIQUID to FCC back again for grain G₃, the free energy at interface is measured to be minimum for IMC grain throughout the simulation. For grain G₂ and G₄, IMC grain evolves and grows in expense of FCC phase by maintaining the minimum free energy at IMC-FCC interface responsible for driving the phase transition.

Figure 10(c) features two subplots with time-temperature graph of the marked point (x) at the IMC interface under \dot{Q}_{min} and \dot{Q}_{max} conditions. It can be observed that the maximum temperature attained by all four interfacial points is greater for \dot{Q}_{max} , compared to \dot{Q}_{min} . Similarly, under maximum heat flux, the time required for the interfacial points to reach maximum temperature and return to ambient temperature is longer than under minimum heat flux condition (380 ms and 300 ms, respectively). Whereas, Figure 10(d) presents the growth of the intermetallic compound's mean

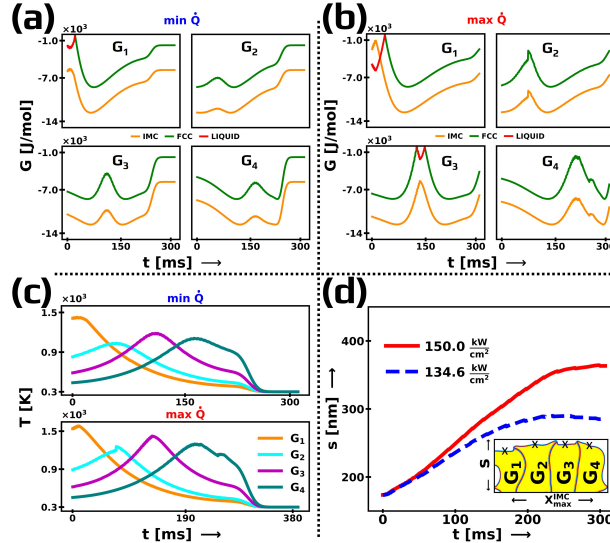


Figure 10: Thermodynamic assessment at the top interface points of four IMC grains G_1 , G_2 , G_3 , G_4 at (a)-(c) for two heat source parameters conditions - $\min \dot{Q}$ (134.6 kW/cm^2 , 5 nm/ms) and $\max \dot{Q}$ (150 kW/cm^2 , 4 nm/ms), reveals that IMC grains having a relatively lower free energy (F) values than FCC phase can grow at the latter's expense. In context of minimum boundary heat source criterion (134.6 kW/cm^2 , 5 nm/ms), as shown in (a) and (c) only the grain G_1 's top interface reaches a higher temperature value ($T > 1337.0 \text{ K}$) at initial time momentarily when LIQUID phase is thermodynamically favorable as compared to the FCC phase. However, in case of maximum boundary heat source criterion (150 kW/cm^2 , 4 nm/ms), as shown in (b) and (c), top interfaces of grains G_1 and G_3 reach the very high temperature condition in which LIQUID phase will momentarily get more favorable conditions than the FCC phase in terms of thermodynamic stability (quantified by the relative values of free energy). At a constant scan speed of 5 nm/ms , the image in (d) shows how a higher irradiance value of laser accelerates the total IMC layer thickness increment rate (s).

thickness (s) on application of two level of laser irradiance at fixed scan-speed of 5 nm/ms . The calculation of mean overall thickness is performed by dividing the total area of IMC grains by the combined bottom width (X_{\max}^{IMC}) of all grains. For laser irradiance of 150 kW/cm^2 the grain growth exhibits a non-linear pattern (red line), featuring an initial surge followed by a plateau towards the simulation's end. Whereas, the growth of intermetallics is not so pronounced for lower laser irradiance (blue dashed line) only attaining a thickness (s) of 289.87 nm at 235.15 ms compared to 289.87 nm at 235.15 ms for higher irradiance level. Here, it can be observed that with just an 11.44% increase in laser irradiance level, the IMC thickness increased by a substantial 25.68% aiding to the conclusion that Ti_3Au intermetallics growth is highly sensitive towards deposited heat.

3.7. Diffusion Kinetics and Lewis Number

In literature, the majority of numerical models for laser processing [53, 54, 58] assume that the melting of material correlates instantaneously with its theoretical melting temperature. This assumption might yield satisfactory results for scenarios where the laser heat source is stationary. However, for a moving laser heat source traversing through the material, the growth of the meltpool cannot simply be a function of temperature alone. Instead, the diffusion of heat and mass transfer come into play for the meltpool to trace the path of the moving laser [89]. Since the diffusion rates of heat and phase (mass) are different quantities, as shown in Equation 25, the assumption that any region inside the domain where the temperature reaches the material's melting point will instantaneously change into meltpool becomes invalid. Thus the movement of the LIQUID phase is dictated by phase diffusion rather than heat diffusion. And since thermal diffusion is faster than phase diffusion [90], it leads to the conclusion that LIQUID phase lags behind the isotherm of melting temperature as laser moves across the domain. To model the real scenario accurately, we quantified the difference between the rates of thermal diffusion and phase diffusion using the Lewis Number (Le), a non-dimensional measure of the thermal-to-phase diffusion ratio, as expressed in Equation 25 [46]. This measure is capable of unraveling the dynamics of laser-induced diffusion fronts in the Ti-Au system.

$$Le_T = \frac{\alpha}{D} = \frac{k_{th}}{\rho Cp} \times \frac{1}{D} \quad (25)$$

where α is the thermal diffusivity, D is the phase diffusivity, k_{th} is the thermal conductivity, Cp denotes the specific heat capacity, and ρ is the density. In the above-mentioned equation subscript 'T' denotes that the associated material property is a function of changing temperature and is not constant during the transient heating via laser irradiance.

To clearly visualize the difference between thermal and phase diffusion phenomena during the simulation, we present Figure 11, where we tracked two diffusion fronts corresponding to the meltpool (\mathfrak{D}) and the melting temperature of 'Au' (1337 K) (τ). Figures 11a and b represent the dynamics of two diffusion fronts for \dot{Q}_{min} and \dot{Q}_{max} conditions at two time frames (11a: $t = 30$ ms, 11b: 175 ms). In the figures, it can be observed that initially at $t = 30$ ms, for both conditions, the gap between thermal and phase diffusion ($\tau - \mathfrak{D}$) is nearly equal. However, as the laser progresses ($t = 175$ ms), for \dot{Q}_{min} the gap increases compared to the \dot{Q}_{max} condition due to the rise in domain temperature with higher heat flux which increases the phase diffusion rate allowing to catch up with thermal front. Figure 11c illustrates the dynamics of the changing Lewis number for the meltpool front and isotherm of 1337 K for all four simulation conditions. From the graph, it can be deduced that the Lewis number is more sensitive to scan speed rather than laser irradiance.

Figures 11d and 11e show the temporal progression of the two diffusion fronts at the top horizontal surface of the domain corresponding to \dot{Q}_{min} and \dot{Q}_{max} conditions. The green line denotes τ (isotherm at $T = 1337$ K) and the blue curve represents the meltpool front (\mathfrak{D}), whereas the positional time lag (δt_{pos}) between τ and \mathfrak{D} is shown by the red curve (Δt_x). The quantity (δt_{pos}) represents the difference in time taken by the thermal front (at 1337 K) and that by the meltpool front to reach a specific coordinate at the top horizontal surface of the numerical domain. Mathematically, it is given by the Expression 26. The simulation videos demonstrating the thermal and phase diffusion lead-lag dynamics, along with plots of positional time-lag over time, are available in the Supplementary Section A. The four videos, which cover combinations of two scan speeds (5 nm/ms and 4 nm/ms) and two irradiance levels (150 kW/cm² and 134.6 kW/cm²), are represented by Videos A9, A10, A11, and A12, respectively.

$$\delta t_{pos} = t_{\mathfrak{D}} - t_{\tau} \quad (26)$$

here, $t_{\mathfrak{D}}$ and t_{τ} are the time taken by phase front and isotherm tip to reach any given spatial coordinate point on the top right surface of the domain. From the Figure 11, we can note that during mid-simulation, the δt_{pos} is lower for the \dot{Q}_{max} condition, meaning the meltpool front catches up with the thermal front faster compared to that during the \dot{Q}_{min} condition. This suggests that the total amount of heat applied to the material dictates the diffusion rate of the LIQUID phase, and the assumption of the thermal melting zone corresponding to the actual meltpool region (i.e., $Le = 1$) becomes valid only when there is high heat deposition to the material.

4. Conclusion

In this research work explores the computational aspect of laser processing parameter's effect on microstructural phase evolution in Ti-Au binary alloy system. Using a temperature-composition dependent free energy formulation for phase-field modelling we conducted four different simulations by varying laser irradiance and scan-speed. The quantitative analysis of thermal history, phase transition, area evolution of phases, meltpool dynamics and kinetics of heat and phase diffusion is performed for combination of different laser parameters. It was observed that the higher laser heat flux condition is highly preferable for the growth of Ti₃Au intermetallic grains and even with the minimum heat flux condition of faster scan-speed at lower irradiance, the IMC grains tend to gradually grow. For FCC and LIQUID phases, they are found to grow in expense of each other as laser melts the Au-rich FCC phase and as laser traverse the LIQUID phase transforms to solid FCC phase, whereas the Ti-rich HCP region continuously shrinks with the evolution of IMC phase at the HCP-FCC interface. The growth of Ti₃Au intermetallics is further backed by minimum value of free energy for intermetallic phase calculated at the contact point between other phases and IMC grains making the Ti₃Au evolution more stable. Further more, we performed numerical analysis on meltpool depth and width with variation in scan-speed and irradiance with result showcasing that higher irradiance at slower scan-speed give rise to a wider and deeper LIQUID phase directly below the laser focus point. Similarly, the quantitative prediction of phase

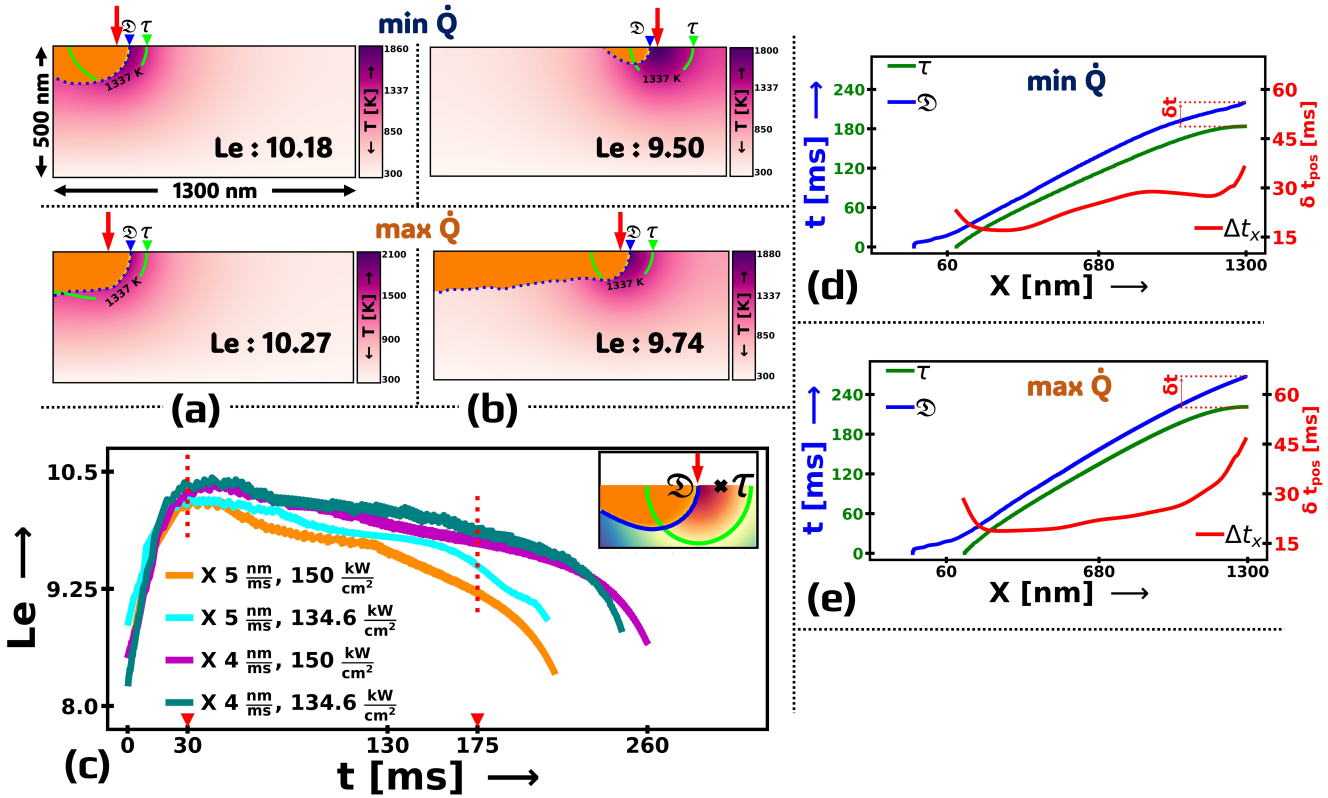


Figure 11: The figures presented herein highlight our key findings regarding the distinction between thermal and phase diffusion fronts, characterized by τ and \mathfrak{D} . In this context, τ marks the isotherm tip corresponding to the FCC-melting temperature (1337 K), while \mathfrak{D} denotes the leading front of the melt pool. Subplots (a) and (b) chronicle the temporal evolution of τ and \mathfrak{D} under minimum and maximum heat flux conditions per unit time, revealing the lead-lag dynamics. For instance, in (a) under \dot{Q}_{\min} (134.6 kW/cm^2 and 5 nm/ms) at $t = 30 \text{ ms}$, the isotherm front (τ) precedes the melt pool front (\mathfrak{D}) with a Lewis number of 10.18 , similar to the \dot{Q}_{\max} (150 kW/cm^2 and 4 nm/ms) scenario at the same time stamp but with a slightly higher Lewis number of 10.27 . In (b), under \dot{Q}_{\min} at $t = 175 \text{ ms}$, the Lewis number decreases to 9.50 , and the laser beam spot surpasses the phase diffusion front τ . Notably, the melt pool area (inside dotted blue line) is distinctly smaller than the region above the melting temperature (green contour line) due to the \dot{Q}_{\min} condition. For \dot{Q}_{\max} at the same time stamp, the melt pool front precedes the laser beam spot, following the thermal front τ with a Lewis number of 9.74 . Plot (c) illustrates the variation in Lewis number for different laser parameters over simulation time, highlighting the significant impact of scanning speed on Lewis number. Slower scanning speeds exhibit higher Lewis numbers, as seen in teal and magenta lines (4 nm/ms), compared to the faster scan speed of 5 nm/ms (orange and light blue lines). The inset schematics provide a visual representation of the thermal front (τ), melt pool front (\mathfrak{D}), and laser beam spot. Graphs (d) and (e) display positional time lags (δt_{pos}) between thermal and melt pool diffusion fronts against the domain's horizontal dimension. Under minimum heat flux per unit time in (d), the melt pool front \mathfrak{D} catches up to the isotherm front τ within 37.08 ms , while in (e) for maximum heat flux per unit time, the positional time lag reaches a maximum of 47.14 ms , as indicated by the red line.

stability between melt pool and HAZ (FCC) region is made via the comparison of free energy values at these regions as laser moves from left top edge to right top edge of the computational domain. Finally, we proceed to address the issue of thermal and phase diffusion difference which are not taken into consideration in contemporary research by calculating the Lewis Number to quantify the differences in phase and thermal diffusion fronts in the domain. We also defined a parameter called *positional time lag* (δt_{pos}) that quantifies the time difference it takes for the phase (melt pool) to catch the isotherm of 1337 K (melting temperature of Au) at the spatial coordinate in the domain by combining the information of Lewis number with the phase-temperature lead-lag dynamics.

In conclusion, our work provides a comprehensive understanding of phase area evolution, free energy dynamics, and diffusion phenomena during laser processing of Ti-Au binary alloy system. With the quantification of interplay between thermal and phase diffusion, we have pushed the boundary of phase field modelling for non-isothermal laser processing, particularly in the context of unique intermetallic compound Ti_3Au . With the preliminary foundation of temperature-composition dependence free energy formulation in this work, we intend to extend this work in future with further refinements in multiphysics by combining surface-tension and other flow phenomenon in the meltpool. We also intend to combine the machine learning model trained on simulation data to construct a Digital Twin capable of taking input from thermal imaging cameras to predict different microstructural features and phase evolution in multi-alloy system.

5. Declarations

The authors declare to have no conflicts of interest that are relevant to the content of this article.

6. Acknowledgment

This work was supported by the National Science Centre, Poland (UMO-2021/42/E/ST5/00339). The resources and services used in this work were provided by the VSC (Flemish Supercomputer Center), funded by the Research Foundation - Flanders (FWO) and the Flemish Government.

7. Data Availability

Codes and data used for this work are available at https://github.com/subediupadeth/MultiPhysics_MultiPhaseField_LaserProcessing.

CRediT authorship contribution statement

Upadeth Subedi: Conceptualization, Methodology, Software, Validation, Formal analysis, Investigation, Data Curation, Writing - Original Draft, Visualization. **Nele Moelans:** Conceptualization, Methodology, Validation, Writing - Review & Editing. **Tomasz Tański:** Validation, Visualization, Writing - Review & Editing, Supervision. **Anil Kunwar:** Methodology, Validation, Data Curation, Supervision, Writing - Review & Editing, Project administration, Funding acquisition.

References

- [1] P. J. Bania, Beta titanium alloys and their role in the titanium industry, *JOM* 46 (1994) 16–19. doi:[10.1007/BF03220742](https://doi.org/10.1007/BF03220742).
- [2] T. S. Tshephe, S. O. Akinwamide, E. Olevsky, P. A. Olubambi, Additive manufacturing of titanium-based alloys- a review of methods, properties, challenges, and prospects, *Heliyon* 8 (2022) e09041. doi:[10.1016/j.heliyon.2022.e09041](https://doi.org/10.1016/j.heliyon.2022.e09041).
- [3] E. Marin, A. Lanzutti, *Biomedical Applications of Titanium Alloys: A Comprehensive Review*, *Materials* 17 (1) (2023) 114. doi:[10.3390/ma17010114](https://doi.org/10.3390/ma17010114).
URL <https://www.mdpi.com/1996-1944/17/1/114>
- [4] E. Lautenschlager, P. Monaghan, *Titanium and titanium alloys as dental materials*, *International dental journal* 43 (3) (1993) 245—253.
URL <http://europepmc.org/abstract/MED/8406955>
- [5] O. Bialas, A. N. Appiah, M. Wala, A. Kunwar, A. Woźniak, P. M. Nuckowski, W. Simka, P. Råback, M. Adamiak, *Laser assisted fabrication of mechanochemically robust Ti_3Au intermetallic at Au-Ti interface*, *Engineering Science and Technology, an International Journal* 42 (2023) 101413. doi:[10.1016/j.jestch.2023.101413](https://doi.org/10.1016/j.jestch.2023.101413).
URL <https://linkinghub.elsevier.com/retrieve/pii/S2215098623000903>
- [6] N. Nohira, W.-T. Chiu, M. Tahara, H. Hosoda, Microstructural changes and mechanical property response to aging heat treatment in hypereutectoid ti-*au*-*mo* biomedical alloys, *Materials Science and Engineering: A* 912 (2024) 146956. doi:[10.1016/j.msea.2024.146956](https://doi.org/10.1016/j.msea.2024.146956).
- [7] J. Liu, K. Wang, X. Li, X. Zhang, X. Gong, Y. Zhu, Z. Ren, B. Zhang, J. Cheng, Biocompatibility and osseointegration properties of a novel high strength and low modulus beta- $ti10mo6zr4sn3nb$ alloy, *Frontiers in Bioengineering and Biotechnology* 11 (2 2023). doi:[10.3389/fbioe.2023.1127929](https://doi.org/10.3389/fbioe.2023.1127929).
- [8] Y. Sun, Q. Liu, Z. Yu, L. Ren, X. Zhao, J. Wang, Study on osseointegration capability of beta-type ti - nb - zr - ta - si alloy for orthopedic implants, *Materials* 17 (2024) 472. doi:[10.3390/ma17020472](https://doi.org/10.3390/ma17020472).
- [9] E. Svanidze, T. Besara, M. Feysi Ozaydin, C. S. Tiwary, J. K. Wang, S. Radhakrishnan, S. Mani, Y. Xin, K. Han, H. Liang, T. Siegrist, P. M. Ajayan, E. Morosan, *High hardness in the biocompatible intermetallic compound b- Ti_3Au* , *Science Advances* 2 (7) (jul 2016).

- [doi:10.1126/sciadv.1600319](https://doi.org/10.1126/sciadv.1600319).
URL <https://www.science.org/doi/10.1126/sciadv.1600319>
- [10] C. C. Lukose, I. Anestopoulos, M. I. Panayiotidis, M. Birkett, Nanomechanical and microstructural characterization of biocompatible ti 3 au thin films grown on glass and ti 6 al 4 v substrates, *ACS Biomaterials Science & Engineering* 10 (2024) 2935–2944. [doi:10.1021/acsbiomaterials.4c00070](https://doi.org/10.1021/acsbiomaterials.4c00070).
- [11] G. B. Kocabas, S. Yalcinkaya, E. Cetin, Y. Sahin, Energy absorption of a novel lattice structure-filled multicell thin-walled tubes under axial and oblique loadings, *Advanced Engineering Materials* 26 (10 2024). [doi:10.1002/adem.202400483](https://doi.org/10.1002/adem.202400483).
- [12] C. C. Lukose, I. Anestopoulos, L. Bowen, M. I. Panayiotidis, M. Birkett, *Atom controlled emergence of high hardness in biocompatible beta-Ti3Au intermetallic thin film surfaces*, *Surfaces and Interfaces* 40 (2023) 103034. [doi:10.1016/j.surfin.2023.103034](https://doi.org/10.1016/j.surfin.2023.103034).
URL <https://linkinghub.elsevier.com/retrieve/pii/S2468023023004042>
- [13] A. Karimi, C. Cattin, *Intermetallic β -Ti3Au hard thin films prepared by magnetron sputtering*, *Thin Solid Films* 646 (2018) 1–11. [doi:10.1016/j.tsf.2017.11.027](https://doi.org/10.1016/j.tsf.2017.11.027).
URL <https://linkinghub.elsevier.com/retrieve/pii/S0040609017308726>
- [14] L. Li, M. Hong, M. Schmidt, M. Zhong, A. Malshe, B. H. in'tVeld, V. Kovalenko, Laser nano-manufacturing – state of the art and challenges, *CIRP Annals* 60 (2011) 735–755. [doi:10.1016/j.cirp.2011.05.005](https://doi.org/10.1016/j.cirp.2011.05.005).
- [15] G. E. Moore, Cramming more components onto integrated circuits, reprinted from electronics, volume 38, number 8, april 19, 1965, pp.114 ff., IEEE Solid-State Circuits Society Newsletter 11 (2006) 33–35. [doi:10.1109/N-SSC.2006.4785860](https://doi.org/10.1109/N-SSC.2006.4785860).
- [16] Y. Zhai, Z. Feng, Y. Zhou, S.-T. Han, Energy-efficient transistors: suppressing the subthreshold swing below the physical limit, *Materials Horizons* 8 (2021) 1601–1617. [doi:10.1039/DOMH02029J](https://doi.org/10.1039/DOMH02029J).
- [17] M. Boutinguiza, A. Riveiro, J. del Val, *Laser Synthesis of Nanomaterials*, MDPI, 2023. [doi:10.3390/books978-3-0365-6928-4](https://doi.org/10.3390/books978-3-0365-6928-4).
- [18] J. Meijer, K. Du, A. Gillner, D. Hoffmann, V. Kovalenko, T. Masuzawa, A. Ostendorf, R. Poprawe, W. Schulz, Laser machining by short and ultrashort pulses, state of the art and new opportunities in the age of the photons, *CIRP Annals* 51 (2002) 531–550. [doi:10.1016/S0007-8506\(07\)61699-0](https://doi.org/10.1016/S0007-8506(07)61699-0).
- [19] R. Srinivasan, E. Sutcliffe, B. Braren, Ablation and etching of polymethylmethacrylate by very short (160 fs) ultraviolet (308 nm) laser pulses, *Applied Physics Letters* 51 (1987) 1285–1287. [doi:10.1063/1.99001](https://doi.org/10.1063/1.99001).
- [20] M. Koleva, A. Dikovska, N. Nedyalkov, T. Genova, G. Atanasova, Laser synthesis and processing of composite nanostructures, *Journal of Chemical Technology and Metallurgy* 59 (2024) 831–839. [doi:10.59957/jctm.v59.i4.2024.11](https://doi.org/10.59957/jctm.v59.i4.2024.11).
- [21] L. Yang, J. Wei, Z. Ma, P. Song, J. Ma, Y. Zhao, Z. Huang, M. Zhang, F. Yang, X. Wang, The fabrication of micro/nano structures by laser machining, *Nanomaterials* 9 (2019) 1789. [doi:10.3390/nano9121789](https://doi.org/10.3390/nano9121789).
- [22] M. Kim, S. Osone, T. Kim, H. Higashi, T. Seto, Synthesis of nanoparticles by laser ablation: A review, *KONA Powder and Particle Journal* 34 (2017) 80–90. [doi:10.14356/kona.2017009](https://doi.org/10.14356/kona.2017009).
- [23] L. Orazi, L. Romoli, M. Schmidt, L. Li, Ultrafast laser manufacturing: from physics to industrial applications, *CIRP Annals* 70 (2021) 543–566. [doi:10.1016/j.cirp.2021.05.007](https://doi.org/10.1016/j.cirp.2021.05.007).
- [24] Y. Rho, C. P. Grigoropoulos, *Laser-Induced Processing of Nanoparticles and Growth of Nanowires*, Springer International Publishing, 2020, pp. 1–39. [doi:10.1007/978-3-319-69537-2_28-1](https://doi.org/10.1007/978-3-319-69537-2_28-1).
- [25] M.-L. Zheng, X.-M. Duan, Laser nano-manufacturing technology and applications towards optical functional nanostructures and devices, in: 2015 Opto-Electronics and Communications Conference (OECC), IEEE, 2015, pp. 1–3. [doi:10.1109/OECC.2015.7340195](https://doi.org/10.1109/OECC.2015.7340195).
- [26] A. Klos, X. Sedao, T. E. Itina, C. Helfenstein-Didier, C. Donnet, S. Peyroche, L. Vico, A. Guignandon, V. Dumas, Ultrafast laser processing of nanostructured patterns for the control of cell adhesion and migration on titanium alloy, *Nanomaterials* 10 (2020) 864. [doi:10.3390/nano10050864](https://doi.org/10.3390/nano10050864).
- [27] J. F. De Almeida, D. C. Amaral, R. T. Coelho, *Innovative Framework to manage New Product Development (NPD) Integrating Additive Manufacturing (AM) and Agile Management*, Procedia CIRP 103 (2021) 128–133. [doi:10.1016/j.procir.2021.10.020](https://doi.org/10.1016/j.procir.2021.10.020).
URL <https://linkinghub.elsevier.com/retrieve/pii/S2212827121008611>
- [28] J. Reichwein, S. Vogel, S. Schork, E. Kirchner, On the Applicability of Agile Development Methods to Design for Additive Manufacturing, *Procedia CIRP* 91 (2020) 653–658. [doi:10.1016/j.procir.2020.03.112](https://doi.org/10.1016/j.procir.2020.03.112).
URL <https://linkinghub.elsevier.com/retrieve/pii/S2212827120308799>
- [29] C. Klahn, B. Leutenecker, M. Meboldt, *Design strategies for the process of additive manufacturing*, *Procedia CIRP* 36 (2015) 230–235. [doi:10.1016/j.procir.2015.01.082](https://doi.org/10.1016/j.procir.2015.01.082).
URL <https://linkinghub.elsevier.com/retrieve/pii/S2212827115008938>
- [30] P. Gradl, D. C. Tinker, A. Park, O. R. Mireles, M. Garcia, R. Wilkerson, C. McKinney, *Robust Metal Additive Manufacturing Process Selection and Development for Aerospace Components*, *Journal of Materials Engineering and Performance* 31 (8) (2022) 6013–6044. [doi:10.1007/s11665-022-06850-0](https://doi.org/10.1007/s11665-022-06850-0).
URL <https://link.springer.com/10.1007/s11665-022-06850-0>
- [31] T. Blachowicz, G. Ehrmann, A. Ehrmann, *Metal Additive Manufacturing for Satellites and Rockets*, *Applied Sciences* 11 (24) (2021) 12036. [doi:10.3390/app112412036](https://doi.org/10.3390/app112412036).
URL <https://www.mdpi.com/2076-3417/11/24/12036>
- [32] M. H. Mobarak, M. A. Islam, N. Hossain, M. Z. Al Mahmud, M. T. Rayhan, N. J. Nishi, M. A. Chowdhury, *Recent advances of additive manufacturing in implant fabrication – A review*, *Applied Surface Science Advances* 18 (2023) 100462. [doi:10.1016/j.apsadv.2023.100462](https://doi.org/10.1016/j.apsadv.2023.100462).
URL <https://linkinghub.elsevier.com/retrieve/pii/S266652392300096X>
- [33] H. B. Mamo, M. Adamiak, A. Kunwar, *3D printed biomedical devices and their applications: A review on state-of-the-art technologies, existing challenges, and future perspectives*, *Journal of the Mechanical Behavior of Biomedical Materials* 143 (2023) 105930. [doi:10.1016/j.jmbbm.2023.105930](https://doi.org/10.1016/j.jmbbm.2023.105930).

- URL <https://linkinghub.elsevier.com/retrieve/pii/S1751616123002837>
- [34] M. Peters, J. Kumpfert, C. Ward, C. Leyens, **Titanium Alloys for Aerospace Applications**, Advanced Engineering Materials 5 (6) (2003) 419–427. doi:[10.1002/adem.200310095](https://doi.org/10.1002/adem.200310095).
URL <https://onlinelibrary.wiley.com/doi/10.1002/adem.200310095>
- [35] P. Nyamekye, S. Rahimpour Golroudbary, H. Piili, P. Luukka, A. Kraslawski, **Impact of additive manufacturing on titanium supply chain: Case of titanium alloys in automotive and aerospace industries**, Advances in Industrial and Manufacturing Engineering 6 (2023) 100112. doi:[10.1016/j.aime.2023.100112](https://doi.org/10.1016/j.aime.2023.100112).
URL <https://linkinghub.elsevier.com/retrieve/pii/S2666912923000016>
- [36] N. H.A. Besisa, T. Yajima, **Titanium-Based Alloys: Classification and Diverse Applications**, in: Titanium-Based Alloys - Characteristics and Applications [Working Title], IntechOpen, 2024. doi:[10.5772/intechopen.1005269](https://doi.org/10.5772/intechopen.1005269).
URL <https://www.intechopen.com/online-first/1180817>
- [37] U. Subedi, N. Moelans, T. Tański, A. Kunwar, **Rapid portabilization of elasto-chemical evolution data for dental Ti-Cr alloy microstructure through sparsification and tensor computation**, Scripta Materialia 244 (2024) 116027. doi:[10.1016/j.scriptamat.2024.116027](https://doi.org/10.1016/j.scriptamat.2024.116027).
URL <https://linkinghub.elsevier.com/retrieve/pii/S1359646224000629>
- [38] S. Pothala, M. Jagannadha Raju, **Recent advances of metallic bio-materials in additive manufacturing in biomedical implants—A review**, Materials Today: Proceedings (jul 2023). doi:[10.1016/j.matpr.2023.07.109](https://doi.org/10.1016/j.matpr.2023.07.109).
URL <https://linkinghub.elsevier.com/retrieve/pii/S2214785323039780>
- [39] Y. Liu, W. Wang, L.-C. Zhang, **Additive manufacturing techniques and their biomedical applications**, Family Medicine and Community Health 5 (4) (2017) 286–298. doi:[10.15212/FMCH.2017.0110](https://doi.org/10.15212/FMCH.2017.0110).
URL <https://fmch.bmj.com/lookup/doi/10.15212/FMCH.2017.0110>
- [40] N. Sommer, P. Kluge, F. Stredak, S. Eigler, H. Hill, T. Niendorf, S. Böhm, **Additive Manufacturing of Compositionally-Graded AISI 316L to CoCrMo Structures by Directed Energy Deposition**, Crystals 11 (9) (2021) 1043. doi:[10.3390/crust11091043](https://doi.org/10.3390/crust11091043).
URL <https://www.mdpi.com/2073-4352/11/9/1043>
- [41] U. Subedi, A. Kunwar, Y. A. Coutinho, K. Gyanwali, **pympealab toolkit for accelerating phase design in multi-principal element alloys**, Metals and Materials International 28 (2022) 269–281. doi:[10.1007/s12540-021-01100-9](https://doi.org/10.1007/s12540-021-01100-9).
URL <https://link.springer.com/10.1007/s12540-021-01100-9>
- [42] U. Subedi, Y. A. Coutinho, P. B. Malla, K. Gyanwali, A. Kunwar, **Automatic featurization aided data-driven method for estimating the presence of intermetallic phase in multi-principal element alloys**, Metals 12 (2022) 964. doi:[10.3390/met12060964](https://doi.org/10.3390/met12060964).
URL <https://www.mdpi.com/2075-4701/12/6/964>
- [43] S. Poudel, U. Subedi, M. O. Hamid, K. Gyanwali, N. Moelans, A. Timofejczuk, A. Kunwar, **Alloymanufacturingnet for discovery and design of hardness-elongation synergy in multi-principal element alloys**, Engineering Applications of Artificial Intelligence 132 (2024) 107902. doi:[10.1016/j.engappai.2024.107902](https://doi.org/10.1016/j.engappai.2024.107902).
- [44] S. Liu, M. Lee, C. Choi, K. Shin, **Effect of additive manufacturing of SUS316L using selective laser melting**, Journal of Materials Research and Technology 24 (2023) 9824–9833. doi:[10.1016/j.jmrt.2023.05.160](https://doi.org/10.1016/j.jmrt.2023.05.160).
URL <https://linkinghub.elsevier.com/retrieve/pii/S2238785423011262>
- [45] S. Ramadugu, S. R. K. Ledella, J. N. J. Gaduturi, R. R. Pinninti, V. Sriram, K. K. Saxena, **Environmental life cycle assessment of an automobile component fabricated by additive and conventional manufacturing**, International Journal on Interactive Design and Manufacturing (IJIDeM) (oct 2023). doi:[10.1007/s12008-023-01532-0](https://doi.org/10.1007/s12008-023-01532-0).
URL <https://link.springer.com/10.1007/s12008-023-01532-0>
- [46] F. Oueslati, B. Ben-Beyaa, T. Lili, **Double-diffusive natural convection and entropy generation in an enclosure of aspect ratio 4 with partial vertical heating and salting sources**, Alexandria Engineering Journal 52 (4) (2013) 605–625. doi:[10.1016/j.aej.2013.09.006](https://doi.org/10.1016/j.aej.2013.09.006).
URL <https://linkinghub.elsevier.com/retrieve/pii/S111001681300094X>
- [47] Y. Yang, O. Ragnvaldsen, Y. Bai, M. Yi, B. X. Xu, **3D non-isothermal phase-field simulation of microstructure evolution during selective laser sintering**, npj Computational Materials 5 (1) (2019) 81. doi:[10.1038/s41524-019-0219-7](https://doi.org/10.1038/s41524-019-0219-7).
URL <https://www.nature.com/articles/s41524-019-0219-7>
- [48] J. Y. Choi, T. Xue, S. Liao, J. Cao, **Accelerating phase-field simulation of three-dimensional microstructure evolution in laser powder bed fusion with composable machine learning predictions**, Additive Manufacturing 79 (2024) 103938. doi:[10.1016/j.addma.2023.103938](https://doi.org/10.1016/j.addma.2023.103938).
URL <https://linkinghub.elsevier.com/retrieve/pii/S2214860423005511>
- [49] D. Liu, Y. Wang, **Mesoscale multi-physics simulation of rapid solidification of Ti-6Al-4V alloy**, Additive Manufacturing 25 (2019) 551–562. doi:[10.1016/j.addma.2018.12.005](https://doi.org/10.1016/j.addma.2018.12.005).
URL <https://linkinghub.elsevier.com/retrieve/pii/S2214860417306139>
- [50] H. Azizi, A. Ebrahimi, N. Ofori-Opoku, M. Greenwood, N. Provatas, M. Mohammadi, **Phase-Field Simulation of Solidification Behavior of AlSi10Mg Alloys Manufactured Through Direct Metal Laser Sintering**, in: Minerals, Metals and Materials Series, 2020, pp. 299–307. doi:[10.1007/978-3-030-36296-6_28](https://doi.org/10.1007/978-3-030-36296-6_28).
URL https://link.springer.com/10.1007/978-3-030-36296-6_28
- [51] A. Kunwar, J. Hektor, S. Nomoto, Y. A. Coutinho, N. Moelans, **Combining multi-phase field simulation with neural network analysis to unravel thermomigration accelerated growth behavior of Cu6Sn5 IMC at cold side Cu–Sn interface**, International Journal of Mechanical Sciences 184 (2020) 105843. doi:[10.1016/j.ijmecsci.2020.105843](https://doi.org/10.1016/j.ijmecsci.2020.105843).
URL <https://linkinghub.elsevier.com/retrieve/pii/S0020740320314466>
- [52] X. Gong, K. Chou, **Phase-Field Modeling of Microstructure Evolution in Electron Beam Additive Manufacturing**, JOM 67 (5) (2015) 1176–1182. doi:[10.1007/s11837-015-1352-5](https://doi.org/10.1007/s11837-015-1352-5).
URL <https://link.springer.com/10.1007/s11837-015-1352-5>

- [53] S. Sahoo, K. Chou, Phase-field simulation of microstructure evolution of Ti–Al–V in electron beam additive manufacturing process, *Additive Manufacturing* 9 (2016) 14–24. doi:10.1016/j.addma.2015.12.005.
URL <https://linkinghub.elsevier.com/retrieve/pii/S2214860415300051>
- [54] R. Darabi, E. Azinpour, A. Reis, J. C. de Sa, Multi-scale Multi-physics Phase-field coupled Thermo-mechanical approach for modeling of powder bed fusion process, *Applied Mathematical Modelling* 122 (2023) 572–597. doi:10.1016/j.apm.2023.06.021.
URL <https://linkinghub.elsevier.com/retrieve/pii/S0307904X23002767>
- [55] S. G. Kim, W. T. Kim, T. Suzuki, Phase-field model for binary alloys, *Physical Review E - Statistical Physics, Plasmas, Fluids, and Related Interdisciplinary Topics* 60 (6) (1999) 7186–7197. doi:10.1103/PhysRevE.60.7186.
URL <https://link.aps.org/doi/10.1103/PhysRevE.60.7186>
- [56] K. Fitzner, O. J. Kleppa, Thermochemistry of binary alloys of transition metals: The Me-Ti, Me-Zr, and Me-Hf(Me = Ag, Au) systems, *Metallurgical Transactions A* 23 (3) (1992) 997–1003. doi:10.1007/BF02675574.
URL <https://link.springer.com/10.1007/BF02675574>
- [57] G. Kim, S. V. Meschel, P. Nash, W. Chen, Experimental formation enthalpies for intermetallic phases and other inorganic compounds, *Scientific Data* 4 (1) (2017) 170162. doi:10.1038/sdata.2017.162.
URL <https://www.nature.com/articles/sdata2017162>
- [58] Z. Li, M. Greenwood, A. Phillion, A phase field methodology for simulating the microstructure evolution during laser powder bed fusion in-situ alloying process, *IOP Conference Series: Materials Science and Engineering* 1281 (1) (2023) 012017. doi:10.1088/1757-899X/1281/1/012017.
URL <https://iopscience.iop.org/article/10.1088/1757-899X/1281/1/012017>
- [59] D. Gaston, C. Newman, G. Hansen, D. Lebrun-Grandié, MOOSE: A parallel computational framework for coupled systems of nonlinear equations, *Nuclear Engineering and Design* 239 (10) (2009) 1768–1778. doi:10.1016/j.nucengdes.2009.05.021.
URL <https://linkinghub.elsevier.com/retrieve/pii/S0029549309002635>
- [60] M. R. Tonks, D. Gaston, P. C. Millett, D. Andrs, P. Talbot, An object-oriented finite element framework for multiphysics phase field simulations, *Computational Materials Science* 51 (1) (2012) 20–29. doi:10.1016/j.commatsci.2011.07.028.
URL <https://linkinghub.elsevier.com/retrieve/pii/S0927025611004204>
- [61] A. D. Lindsay, D. R. Gaston, C. J. Permann, J. M. Miller, D. Andrš, A. E. Slaughter, F. Kong, J. Hansel, R. W. Carlsen, C. Icenhour, L. Harbour, G. L. Giudicelli, R. H. Stogner, P. German, J. Badger, S. Biswas, L. Chapuis, C. Green, J. Hales, T. Hu, W. Jiang, Y. S. Jung, C. Matthews, Y. Miao, A. Novak, J. W. Peterson, Z. M. Prince, A. Rovinelli, S. Schunert, D. Schwen, B. W. Spencer, S. Veeraraghavan, A. Recuero, D. Yushu, Y. Wang, A. Wilkins, C. Wong, 2.0 - MOOSE: Enabling massively parallel multiphysics simulation, *SoftwareX* 20 (2022) 101202. doi:10.1016/j.softx.2022.101202.
URL <https://linkinghub.elsevier.com/retrieve/pii/S2352711022001200>
- [62] D. Gu, Laser Additive Manufacturing (AM): Classification, Processing Philosophy, and Metallurgical Mechanisms, in: *Laser Additive Manufacturing of High-Performance Materials*, Springer Berlin Heidelberg, Berlin, Heidelberg, 2015, pp. 15–71. doi:10.1007/978-3-662-46089-4_2.
URL https://link.springer.com/10.1007/978-3-662-46089-4_2
- [63] N. Moelans, A quantitative and thermodynamically consistent phase-field interpolation function for multi-phase systems, *Acta Materialia* 59 (3) (2011) 1077–1086. doi:10.1016/j.actamat.2010.10.038.
URL <https://linkinghub.elsevier.com/retrieve/pii/S1359645410007019>
- [64] C. N. Singman, Atomic volume and allotropy of the elements, *Journal of Chemical Education* 61 (2) (1984) 137–142. doi:10.1021/ED061P137.
URL <https://pubs.acs.org/doi/abs/10.1021/ed061p137>
- [65] W. H. Xiong, W. Liu, M. M. Dai, J. Q. Liu, X. G. Lu, Assessments of molar volumes of Co-, Ni- and Ti-related bcc and fcc phases, *Calphad: Computer Coupling of Phase Diagrams and Thermochemistry* 66 (2019) 101629. doi:10.1016/j.calphad.2019.101629.
URL <https://linkinghub.elsevier.com/retrieve/pii/S0364591619300896>
- [66] A. Kunwar, Y. A. Coutinho, J. Hektor, H. Ma, N. Moelans, Integration of machine learning with phase field method to model the electromigration induced Cu₆Sn₅ IMC growth at anode side Cu/Sn interface, *Journal of Materials Science and Technology* 59 (2020) 203–219. doi:10.1016/j.jmst.2020.04.046.
URL <https://linkinghub.elsevier.com/retrieve/pii/S1005030220305156>
- [67] A. Kunwar, E. Yousefi, X. Zuo, Y. Sun, D. Seveno, M. Guo, N. Moelans, Multi-phase field simulation of Al₃Ni₂ intermetallic growth at liquid Al/solid Ni interface using MD computed interfacial energies, *International Journal of Mechanical Sciences* 215 (2022) 106930. doi:10.1016/j.ijmecsci.2021.106930.
URL <https://www.sciencedirect.com/science/article/pii/S0020740321006408> <https://linkinghub.elsevier.com/retrieve/pii/S0020740321006408>
- [68] J. Hektor, M. Ristinmaa, H. Hallberg, S. A. Hall, S. Iyengar, Coupled diffusion-deformation multiphase field model for elastoplastic materials applied to the growth of Cu₆Sn₅, *Acta Materialia* 108 (2016) 98–109. doi:10.1016/j.actamat.2016.02.016.
URL <https://linkinghub.elsevier.com/retrieve/pii/S1359645416300933>
- [69] S. Zhu, T. P. Chen, Z. H. Cen, E. S. M. Goh, S. F. Yu, Y. C. Liu, Y. Liu, Split of surface plasmon resonance of gold nanoparticles on silicon substrate: a study of dielectric functions, *Optics Express* 18 (21) (2010) 21926. doi:10.1364/OE.18.021926.
URL <https://opg.optica.org/oe/abstract.cfm?uri=oe-18-21-21926>
- [70] D. Hwang, S. G. Ryu, N. Misra, H. Jeon, C. P. Grigoropoulos, Nanoscale laser processing and diagnostics, *Applied Physics A: Materials Science and Processing* 96 (2009) 289–306. doi:10.1007/s00339-009-5207-1.
- [71] A. P. Joglekar, H. hua Liu, E. Meyhöfer, G. Mourou, A. J. Hunt, Optics at critical intensity: Applications to nanomorphing, *Proceedings of the National Academy of Sciences* 101 (2004) 5856–5861. doi:10.1073/pnas.0307470101.

- [72] K. Sugioka, Progress in ultrafast laser processing and future prospects, *Nanophotonics* 6 (2017) 393–413. [doi:10.1515/nanoph-2016-0004](https://doi.org/10.1515/nanoph-2016-0004).
- [73] J. W. Peterson, A. D. Lindsay, F. Kong, **Overview of the incompressible Navier–Stokes simulation capabilities in the MOOSE framework**, *Advances in Engineering Software* 119 (2018) 68–92. [doi:10.1016/j.advengsoft.2018.02.004](https://doi.org/10.1016/j.advengsoft.2018.02.004).
URL <https://linkinghub.elsevier.com/retrieve/pii/S0965997817310591>
- [74] A. Kunwar, L. An, J. Liu, S. Shang, P. Råback, H. Ma, X. Song, **A data-driven framework to predict the morphology of interfacial Cu₆Sn₅ IMC in SAC/Cu system during laser soldering**, *Journal of Materials Science and Technology* 50 (2020) 115–127. [doi:10.1016/j.jmst.2019.12.036](https://doi.org/10.1016/j.jmst.2019.12.036).
URL <https://linkinghub.elsevier.com/retrieve/pii/S1005030220302279>
- [75] A. Jain, S. P. Ong, G. Hautier, W. Chen, W. D. Richards, S. Dacek, S. Cholia, D. Gunter, D. Skinner, G. Ceder, K. A. Persson, **Commentary: The Materials Project: A materials genome approach to accelerating materials innovation**, *APL Materials* 1 (1) (jul 2013). [doi:10.1063/1.4812323](https://doi.org/10.1063/1.4812323).
URL <https://legacy.materialsproject.org/materials/mp-1786/>
- [76] R. Powell, R. Tye, The thermal and electrical conductivity of titanium and its alloys, *Journal of the Less Common Metals* 3 (1961) 226–233. [doi:10.1016/0022-5088\(61\)90064-9](https://doi.org/10.1016/0022-5088(61)90064-9).
- [77] A. Khvan, I. Uspenskaya, N. Aristova, Q. Chen, G. Trimarchi, N. Konstantinova, A. Dinsdale, **Description of the thermodynamic properties of pure gold in the solid and liquid states from 0 K**, *Calphad* 68 (2020) 101724. [doi:10.1016/j.calphad.2019.101724](https://doi.org/10.1016/j.calphad.2019.101724).
URL <https://linkinghub.elsevier.com/retrieve/pii/S0364591619302858>
- [78] J. Chase, MW, **NIST-JANAF thermochemical tables, monograph 9**, fourth edi Edition, Vol. 9, American Chemical Society, Washington DC, 1998.
URL <https://webbook.nist.gov/cgi/inchi?ID=C7440326&Type=JANAFS&Table=on>
- [79] W. Luo, Z. Jin, H. Liu, T. Wang, **Thermodynamic assessment of the Au-Ti system**, *Calphad: Computer Coupling of Phase Diagrams and Thermochemistry* 25 (1) (2001) 19–26. [doi:10.1016/S0364-5916\(01\)00026-8](https://doi.org/10.1016/S0364-5916(01)00026-8).
URL <https://linkinghub.elsevier.com/retrieve/pii/S0364591601000268>
- [80] T. Dubberstein, M. Schürmann, H. Chaves, H. P. Heller, C. G. Aneziris, **A Novel Vibrating Finger Viscometer for High-Temperature Measurements in Liquid Metals and Alloys**, *International Journal of Thermophysics* 37 (10) (2016) 100. [doi:10.1007/s10765-016-2104-7](https://doi.org/10.1007/s10765-016-2104-7).
URL <http://link.springer.com/10.1007/s10765-016-2104-7>
- [81] N. Zhao, Y. Zhong, M. Huang, H. Ma, W. Dong, Growth kinetics of cu₆sn₅ intermetallic compound at liquid-solid interfaces in cu/sn/cu interconnects under temperature gradient, *Scientific Reports* 5 (2015) 13491. [doi:10.1038/srep13491](https://doi.org/10.1038/srep13491).
- [82] G. E. Bean, D. B. Witkin, T. D. McLouth, D. N. Patel, R. J. Zaldivar, **Effect of laser focus shift on surface quality and density of Inconel 718 parts produced via selective laser melting**, *Additive Manufacturing* 22 (2018) 207–215. [doi:10.1016/j.addma.2018.04.024](https://doi.org/10.1016/j.addma.2018.04.024).
URL <https://linkinghub.elsevier.com/retrieve/pii/S2214860417303044>
- [83] R. R. Mohanty, J. E. Guyer, Y. H. Sohn, **Diffusion under temperature gradient: A phase-field model study**, *Journal of Applied Physics* 106 (3) (2009). [doi:10.1063/1.3190607](https://doi.org/10.1063/1.3190607).
- [84] T. D. Oyedeleji, Y. Yang, H. Egger, B. X. Xu, **Variational quantitative phase-field modeling of nonisothermal sintering process**, *Physical Review E* 108 (2) (2023). [doi:10.1103/PhysRevE.108.025301](https://doi.org/10.1103/PhysRevE.108.025301).
- [85] M. Parsazadeh, S. Sharma, N. Dahotre, **Towards the next generation of machine learning models in additive manufacturing: A review of process dependent material evolution**, *Progress in Materials Science* 135 (2023) 101102. [doi:10.1016/j.pmatsci.2023.101102](https://doi.org/10.1016/j.pmatsci.2023.101102).
- [86] R. R. Kamath, H. Choo, K. Fezzaa, S. S. Babu, **Estimation of spatio-temporal temperature evolution during laser spot melting using in situ dynamic x-ray radiography**, *Metallurgical and Materials Transactions A* (2 2024). [doi:10.1007/s11661-024-07307-w](https://doi.org/10.1007/s11661-024-07307-w).
- [87] W. Liu, J. DuPont, **Effects of melt-pool geometry on crystal growth and microstructure development in laser surface-melted superalloy single crystals**, *Acta Materialia* 52 (16) (2004) 4833–4847. [doi:10.1016/j.actamat.2004.06.041](https://doi.org/10.1016/j.actamat.2004.06.041).
URL <https://linkinghub.elsevier.com/retrieve/pii/S1359645404003908>
- [88] Y. Li, K. Zhou, S. B. Tor, C. K. Chua, K. F. Leong, **Heat transfer and phase transition in the selective laser melting process**, *International Journal of Heat and Mass Transfer* 108 (2017) 2408–2416. [doi:10.1016/j.ijheatmasstransfer.2017.01.093](https://doi.org/10.1016/j.ijheatmasstransfer.2017.01.093).
URL <https://linkinghub.elsevier.com/retrieve/pii/S0017931016330290>
- [89] X. Shi, D. Gu, Y. Li, D. Dai, Q. Ge, Y. Sun, H. Chen, **Thermal behavior and fluid dynamics within molten pool during laser inside additive manufacturing of 316L stainless steel coating on inner surface of steel tube**, *Optics and Laser Technology* 138 (2021) 106917. [doi:10.1016/j.optlastec.2021.106917](https://doi.org/10.1016/j.optlastec.2021.106917).
URL <https://linkinghub.elsevier.com/retrieve/pii/S0030399221000050>
- [90] N. Provatas, K. Elder, **Phase-Field Methods in Materials Science and Engineering**, Wiley, 2010. [doi:10.1002/9783527631520](https://doi.org/10.1002/9783527631520).
URL <https://onlinelibrary.wiley.com/doi/book/10.1002/9783527631520>

A. Appendix: Video animation of numerical simulations

All the videos file are provided as supplementary material during the submission. They are also available at the GitHub repository mentioned in Section 7.

Video A1: Thermal History

The video should appear here in the online version.

[Click Here: Irradiance: 150 kW/cm² & Scan-Speed 5nm/ms](#)

Caption: Video animation shows the thermal history (temperature distribution) across the computational domain when the laser with Irradiance of 150 kW/cm² is applied at the top surface from left to right at a scan speed of 5nm/ms.

Video A2: Thermal History

The video should appear here in the online version.

[Click Here: Irradiance: 150 kW/cm² & Scan-Speed 4nm/ms](#)

Caption: Video animation shows the thermal history (temperature distribution) across the computational domain when the laser with Irradiance of 150 kW/cm² is applied at the top surface from left to right at a scan speed of 4nm/ms.

Video A3: Thermal History

The video should appear here in the online version.

[Click Here: Irradiance: 134.6 kW/cm² & Scan-Speed 5nm/ms](#)

Caption: Video animation shows the thermal history (temperature distribution) across the computational domain when the laser with Irradiance of 134.6 kW/cm² is applied at the top surface from left to right at a scan speed of 5nm/ms.

Video A4: Thermal History

The video should appear here in the online version.

[Click Here: Irradiance: 134.6 kW/cm² & Scan-Speed 4nm/ms](#)

Caption: Video animation shows the thermal history (temperature distribution) across the computational domain when the laser with Irradiance of 134.6 kW/cm² is applied at the top surface from left to right at a scan speed of 4nm/ms.

Video A5: Phase Evolution

The video should appear here in the online version.

[Click Here: Irradiance: 150 kW/cm² & Scan-Speed 5nm/ms](#)

Caption: Video animation shows the evolution of different microstructural phases in the computational domain on application of laser heat source with an Irradiance of 150 kW/cm² at the top surface with a scan speed of 5nm/ms. The blue contour line represents the temperature information at those coordinates.

Video A6: Phase Evolution

The video should appear here in the online version.

[Click Here: Irradiance: 150 kW/cm² & Scan-Speed 4nm/ms](#)

Caption: Video animation shows the evolution of different microstructural phases in the computational domain on application of laser heat source with an Irradiance of 150 kW/cm² at the top surface with a scan speed of 4nm/ms. The blue contour line represents the temperature information at those coordinates.

Video A7: Phase Evolution

The video should appear here in the online version.

[Click Here: Irradiance: 134.6 kW/cm² & Scan-Speed 5nm/ms](#)

Caption: Video animation shows the evolution of different microstructural phases in the computational domain on application of laser heat source with an Irradiance of 134.6 kW/cm² at the top surface with a scan speed of 5nm/ms. The blue contour line represents the temperature information at those coordinates.

Video A8: Phase Evolution

The video should appear here in the online version.

[Click Here: Irradiance: 134.6 kW/cm² & Scan-Speed 4nm/ms](#)

Caption: Video animation shows the evolution of different microstructural phases in the computational domain on

application of laser heat source with an Irradiance of 134.6 kW/cm^2 at the top surface with a scan speed of 4nm/ms. The blue contour line represents the temperature information at those coordinates.

Video A9: : Isotherm

The video should appear here in the online version.

[Click Here: Irradiance: 150 kW/cm² & Scan-Speed 5nm/ms](#)

Caption: Video animation illustrates the lead-lag dynamics of meltpool phase diffusion front to that of thermal diffusion front (Isotherm). The laser parameter are as follows, Irradiance: 150 kW/cm^2 | Scan speed: 5nm/ms. The inset animation sequence shows the time lag for phase front to reach thermal front at a certain coordinate of space.

Video A10: : Isotherm

The video should appear here in the online version.

[Click Here: Irradiance: 150 kW/cm² & Scan-Speed 4nm/ms](#)

Caption: Video animation illustrates the lead-lag dynamics of meltpool phase diffusion front to that of thermal diffusion front (Isotherm). The laser parameter are as follows, Irradiance: 150 kW/cm^2 | Scan speed: 4nm/ms. The inset animation sequence shows the time lag for phase front to reach thermal front at a certain coordinate of space.

Video A11: : Isotherm

The video should appear here in the online version.

[Click Here: Irradiance: 134.6 kW/cm² & Scan-Speed 5nm/ms](#)

Caption: Video animation illustrates the lead-lag dynamics of meltpool phase diffusion front to that of thermal diffusion front (Isotherm). The laser parameter are as follows, Irradiance: 134.6 kW/cm^2 | Scan speed: 5nm/ms. The inset animation sequence shows the time lag for phase front to reach thermal front at a certain coordinate of space.

Video A12: Isotherm

The video should appear here in the online version.

[Click Here: Irradiance: 134.6 kW/cm² & Scan-Speed 4nm/ms](#)

Caption: Video animation illustrates the lead-lag dynamics of meltpool phase diffusion front to that of thermal diffusion front (Isotherm). The laser parameter are as follows, Irradiance: 134.6 kW/cm^2 | Scan speed: 4nm/ms. The inset animation sequence shows the time lag for phase front to reach thermal front at a certain coordinate of space.